Multi-temperature Electron Density Studies

Chapter 19
Multi-temperature Electron Density Studies*

Riccardo Destro, Leonardo Lo Presti, Raffaella Soave, and Andrés E. Goeta

19.1 Introduction

To obtain accurate experimental electron densities $\rho(\mathbf{r})$ it is mandatory to perform a reliable deconvolution of the static electron density distribution (EDD) from thermal motion. To this end, single-crystal X-ray diffraction (XRD) experiments, especially on molecular crystals, have to be performed at low temperature. Under these conditions enough high-order diffraction data – which contain information on the core electrons – become measurable, allowing an appropriate treatment of the thermal motion. Chapter 3 deals with this problem; it describes atomic displacements in crystals in the harmonic approximation and beyond, and comments on recently developed methods that combine experimental and theoretical information to achieve deconvolution. In the present chapter, the effects of temperature on the experimental electron densities are examined from a more general perspective.

A firm tenet in the charge density community, apropos of temperature, is "the lower the better" [1]. This recommendation derives from at least three reasons: (i) more reliable determination of the static $\rho(\mathbf{r})$; (ii) lower values of the corre-

* To their great sorrow, Riccardo Destro, Leonardo Lo Presti and Raffaella Soave announce the death of Dr. Andrés E. Goeta on July 29th, 2011.

R. Destro (✉) • L. Lo Presti
Department of Physical Chemistry and Electrochemistry, Università degli Studi di Milano, Via Golgi 19, 20133 Milan, Italy
e-mail: riccardo.destro@unimi.it; leonardo.lopresti@unimi.it

R. Soave
Istituto di Scienze e Tecnologie Molecolari (ISTM), Italian National Reseearch Council (CNR), Via Golgi 19, 20133 Milan, Italy
e-mail: raffaella.soave@istm.cnr.it

A.E. Goeta
Chemistry Department, Durham University, South Road, Durham, DH1 3LE UK
e-mail: a.e.goeta@durham.ac.uk

lation coefficients between positional/thermal parameters and electron population coefficients of generalized scattering factors; (iii) higher precision, i.e. smaller estimated standard deviations (esd's), of the refined parameters, and hence of all the electrostatic properties derived from $\rho(\mathbf{r})$. However, what is the quantitative gain in accuracy and precision when collecting data below, say, the liquid nitrogen temperature? Furthermore, is it possible to establish an upper limit on the temperature, above which experiments aimed at a reliable determination of the electron density are not worth the effort? Possible answers to these questions are critically examined in the next Section, through examples taken from the pertinent literature.

A change in the temperature can also give rise to a significant change in the interactions between the molecules. The lowering of T causes the reduction of the overall thermal motion in the crystal, decreasing the amplitudes of both the molecular and the lattice vibration modes. Moreover, the intermolecular (interatomic) potential due to the crystal field changes because of the lattice shrinking[1] [2] and, at the same time, less and less states become thermally accessible in the crystal. The reduction of the vibration amplitudes makes the molecules approach each other, strengthening all the interactions (both attractive and repulsive) between them. The change of the potential and the reduction of the thermally accessible regions of the potential energy surface may drive the molecules into energy minima that correspond to a conformation or packing different from that observed at room temperature. In the last case, a structural phase transition occurs, considerably altering the intermolecular interactions. If the experimental EDD is available above and below the transition temperature T_{tr}, it is possible to gain insight into the observed structural changes by relating them to the changes of the scalar field $\rho(\mathbf{r})$ itself. To this end, the Quantum Theory of Atoms in Molecules (QTAIM) [3, 4] illustrated in Chaps. 1, 9 and 12 provides useful topological tools to describe the nature of the chemical interactions and the corresponding changes which occur as a function of T. Moreover, a change in the temperature can vary the population of electronic states. This is particularly well-known in the field of spin crossover (SCO) materials, which are molecular compounds with the ability to switch between a paramagnetic high spin state (HS) and a diamagnetic low-spin ground state (LS) [5].

Special attention is required when comparing the experimental EDD above and below T_{tr}, because in most cases the $\rho(\mathbf{r})$ obtained above T_{tr} shows intrinsically lower precision than the $\rho(\mathbf{r})$ obtained at $T < T_{tr}$, for the reasons mentioned above. In addition further difficulties may arise, e.g. both phases [6] or at least the high-T one [7] may be disordered, there may be hysteresis effects [8], twinning [6, 9], or coexistence of phases [10]. All these problems hamper or even prevent the determination of accurate experimental electron densities, even at very low T. However, if enough single-crystal XRD data are available to at least solve the structure with satisfactory accuracy, such a structure may serve as a starting point

---

[1]In negative thermal expansion materials (such as ZrW_2O_8 or HfW_2O_8) [2] the effect of the T lowering is just the opposite, i.e. it implies an expansion, rather than a shrinking, of the lattice. See also Chap. 17.

for theoretical periodic quantum calculations in both the high-T and the low-T phases. QTAIM can then be applied to the theoretical $\rho(\mathbf{r})$ above and below T_{tr} and the transition can be followed topologically. Such solid-state simulations may be performed with the CRYSTAL or the ESPRESSO codes described in Chap. 2 and with other publicly available software [11, 12]. On the other hand, when both experimental and theoretical results are available, it is important to compare them on the same grounds. For instance, it could be useful to project the theoretical EDD onto a set of Fourier-calculated structure factor amplitudes, which can then be examined by a conventional multipole model and easily compared with the experiment-derived ones.

Sections 19.3 and 19.4 deal with the T-dependent phenomena described above. In Sect. 19.3, the interplay between $\rho(\mathbf{r})$ and other physical properties as a function of T is considered, and some cases are presented for which the EDD is available (experimentally or theoretically) both above and below the transition temperature. Sect. 19.4 will then be devoted to the changes in $\rho(\mathbf{r})$ associated with spin transitions, i.e. changes linked to an intra-ionic move of electrons between non-bonding and anti-bonding orbitals and structurally reflected in the metal to ligand distances.

19.2 The Role of Temperature in Accurate Experimental Charge-Density Studies

Multi-temperature studies of crystalline structures can be carried out for a variety of purposes, which include the accurate analysis of molecular thermal motion in crystals [13, 14], the explicit search for structural phase transitions [15, 16], the investigation of the effect of T on the *intra-* [17, 18] and *inter-* [19] molecular interactions and on hydrogen bonding [17, 18, 20], and the search for the best conditions to accurately evaluate the electron density.

In early investigations, when the experimental analysis of EDD was still a challenge, one of the main targets was the determination of the so-called difference Fourier synthesis, defined as:

$$\Delta\rho = 1/V\sum_{hkl}\Delta F\,(hkl)\exp\left[-i\phi_{hkl}\right] = 1/V\sum_{hkl}\left(|F_o\,(hkl)| - |F_c\,(hkl)|\right)\exp\left[-i\phi_{hkl}\right]$$

(19.1)

where V is the unit cell volume, $|F_o(hkl)|$ and $|F_c(hkl)|$ are the observed and calculated structure factor amplitudes, respectively, and ϕ_{hkl} is the phase of F_c. As the structure factors were computed using spherical-atom form factors, they could not account for the local deformation of the electron charge cloud due to chemical bonding. Provided that all the atoms were correctly included in the structure
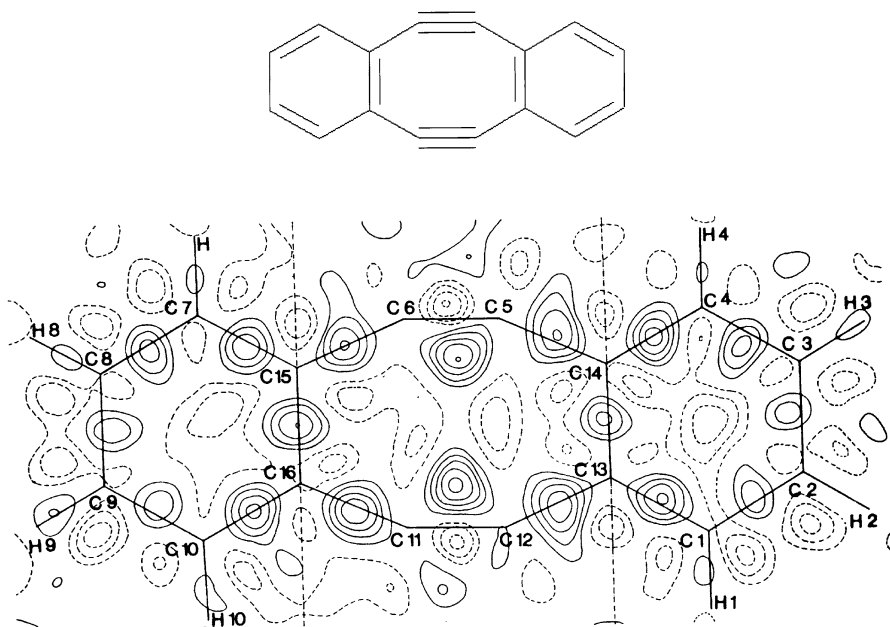
Fig. 19.1 Sections of the ΔF syntheses showing residual electron density at $T = 113$ K. The three sections of the composite, separated by chain-dotted lines, are defined by the planes through the benzene rings and the plane through the triple bonds. Contour levels at intervals of 0.05 e·Å^{-3}. *Solid lines* positive; *dashed lines* negative; zero contours omitted

(i.e. there were no missing, no misassigned nor misplaced atoms), the $\Delta\rho$ maps revealed just those features of $\rho(\mathbf{r})$ that are related to the bonding. These features were indeed present in the observed data, but were not modelled by the structure factors calculated with spherical-atom form factors. Before the era of the multipole formalisms [21–23], the interpretation of such maps was the main method employed to extract experimental information on the chemical bonds from XRD data. Because the F_o magnitudes depend on the thermal motion in the crystal through the Debye-Waller factors, the lower the data collection temperature, the more informative the corresponding $\Delta\rho$ maps. When *sym*-dibenzo-1,5-cyclooctadiene-3,7-diyne, for example, was studied at $T = 290$, 218 and 113 K [24], it was found that the most interesting difference-Fourier features concern the central eight-membered ring, and particularly the region close to the two triple bonds, where both negative and positive residues are clearly visible (see Fig. 19.1). While the negative holes were ascribed to the inadequacy of the spherical atom scattering factor formalism, the positive peaks were rationalized by invoking an asymmetrical distribution of the electron charge density of the formal triple bonds, in agreement with the results of theoretical calculations. These features were less and less apparent when the same map was obtained from data sets collected at 218 K and 290 K (see Fig. 5 in Ref. [24]),

indicating that the lowering of T was mandatory to achieve both qualitative and quantitative information on the chemical bonds.

19.2.1   The Problems of Deconvolution and Correlations Between Parameters

An alternative $\Delta\rho$, the so-called static model deformation density, is nowadays preferred to that obtained by difference Fourier synthesis. This static $\Delta\rho$ is defined [25] as

$$\Delta\rho = \rho_{\text{model}} - \rho_{\text{free atom}} \qquad (19.2)$$

where ρ_{model} is the sum of model density functions, which are usually atom-centred multipole functions as in the formalism developed by Stewart [21] or by Hansen and Coppens [23]; $\rho_{\text{free atom}}$ is the reference spherical density of the free atoms held at the same positions as the multipole atoms. Like the earlier difference Fourier map, this $\Delta\rho$ also maps the electronic rearrangement occurring upon formation of chemical bonds, but now the atoms are "frozen" at well defined positions, i.e. the thermal motion is supposed to have been completely deconvoluted from the deformation density (see also Chap. 3).

Deformation densities are not the only tool – in the experimental charge density field – to investigate chemical bonding properties: the development of the QTAIM [3, 4] has triggered a great deal of effort to obtain reliable *total* $\rho(\mathbf{r})$'s with the help of the above mentioned multipole models. Accurate $\rho(\mathbf{r})$'s are actually the main target of modern low-T XRD experiments, and the well-known severe requirements for the evaluation of high-quality total $\rho(\mathbf{r})$ from single-crystal XRD data are continuously investigated [26]. Optimal sample quality [27], high redundancy, large number and high precision of measurements, especially at high angle, are all needed for a proper treatment of the thermal motion, to reduce the least-squares correlations between parameters and to avoid slow convergence and poor-quality (in terms of precision) of the final multipole coefficients. Unfortunately, it is not always possible to accomplish these goals with the available experimental data, particularly because the number of laboratories equipped with in-home cryogenic systems capable to reach very low temperatures ($T < 50$ K) is quite limited.

Two questions are of particular relevance in this context: (i) are the multipole parameters transferable? If a precise and accurate set of multipole coefficients is obtained from a low-T XRD experiment, with what confidence can such parameters be employed to model the EDD of the same substance at another (higher) temperature? (ii) How low must the temperature of the data collection be to achieve a satisfactory deconvolution of the thermal motion from the static deformation density? The next subsections present some attempts to answer these questions.

19.2.2   Transferability of Low-T Multipole Parameters on High-T Structures

In the absence of T-dependent chemical or physical transformations, the *static*[2] molecular EDD is not influenced by the temperature. As a consequence, properties like the atomic charges, the molecular electrostatic moments, and the nature of the *intramolecular* chemical bonds (to mention but a few), are expected not to vary by changing T. Hence, if accurate multipole parameters are known from low-T experiments, it is reasonable to assume that they could be employed at higher temperatures on the same substance, for instance to get a better description of its thermal motion. Furthermore, the topological properties of $\rho(\mathbf{r})$ should also be transferable between similar molecules, according to the well-known QTAIM [3] assumption of atoms as building blocks of chemical systems. This implies that the multipole parameters should be, at least to some extent, transferable also between chemically similar substances, even when they are studied at different temperatures.

The pioneering work by Pratt-Brock, Dunitz and Hirshfeld in 1991 explored this possibility [28]. They transferred the atomic charge-deformation parameters obtained by applying the Hirshfeld formalism [22] on extensive XRD data (up to $\sin\vartheta/\lambda = 1.26\,\text{Å}^{-1}$) of perylene at 83 K to naphtalene and anthracene. The main scope of that work was to improve the temperature-dependent ADP's that were originally derived by conventional least-squares analyses from XRD data of moderate resolution (up to $\sin\vartheta/\lambda = 0.65\,\text{Å}^{-1}$) at temperatures in the range 92–239 K for naphtalene and 94–295 K for anthracene. Although the authors admitted that it was not possible to answer with complete confidence whether the "use of transferred deformation densities has actually led to *improved* values of the atomic ADP's", they were among the first to develop a method for transferring experimentally derived deformation densities between chemically related molecules.

Several other recent works have nowadays assessed the transferability of multipole parameters. Mata et al., for instance, obtained the EDD of L-histidinium dihydrogen orthophosphate orthophosphoric acid from X-ray and neutron diffraction data at $T = 120$ K; then, they collected another set of diffraction data at $T = 294$ K on the same substance and successfully interpreted them using the low-T EDD [29]. Furthermore, transferability between chemically related substances is the underlying idea of the data bank of experimental aspherical atom parameters, applicable to charge density studies of macromolecules of biological interest (such as polypeptides) [30–32]. This topic is discussed in some detail in Chap. 15.

---

[2]The "static" EDD corresponding to an energy minimum of the potential energy surface at $T = 0$ K is just a *model*, i.e. a purely theoretical concept. Nevertheless, it supplies sensible and reliable information on the nature of the chemical interactions in molecules, being characteristic of a *specific* chemical system.

19.2.3   Setting an Upper Limit on the Temperature?

Once an exhaustive, accurate and adequately phased single-crystal XRD data set has been obtained, the main problem, even if the experiment was performed at low temperature, is to assess whether the final experimental EDD is free of errors due to an insufficient treatment of thermal motion.

Several experimental works (mostly on organic or organometallic substances) have been devoted to this topic; here we comment only on a few of them. Sometimes the multi-temperature data collections have been carried out with a single experimental setup, one of the main focuses being just the deconvolution problem [33, 34]; sometimes the performances of different experimental setups (including synchrotron X-ray sources [35–38]) for an accurate EDD determination have been examined. In all these works the XRD data sets have been collected at T not higher than ∼200 K.

Two recent studies by Overgaard et al. [37, 38] compare the structural and electronic properties of polynuclear organometallic complexes as obtained from synchrotron data at T < 20 K and from conventional X-ray sources at 100 K. For one complex, $Co_2(CO)_6(HC{\equiv}CC_6H_{10}OH)$ [37], the two data sets were compared on the basis of the EDD properties at all bond critical points (bcp's). The authors report that "this approach indicates quite different densities from the two data sets", mostly due to significant differences in the carbonyl bonds, for which a small shift (∼0.03 Å towards C) in the position of the bcp was found for the synchrotron data set. A detailed comparison with the theoretical electron density showed that the synchrotron data were to be preferred, even though the conventional data provided results closer to theory for certain integrated properties (e.g. the atomic charges on Co). Similarly, preference to 15 K synchrotron data was given in the case of another complex $[(Fe_3O(HCOO)_6(HCOO)_3]^{2-}{\cdot}H_2O{\cdot}2(\alpha\text{-}CH_3NC_5H_5)^+$, [38]), for which relevant discrepancies between the EDD results from the two data sets were also found, particularly in $\rho(\mathbf{r})$ and its Laplacian at the bcp's. All this did not prevent the authors from concluding that "two independent high-resolution studies, including one using an intense synchrotron source in combination with very low temperatures, lead to comparable results" [38]. The conclusion that "the errors in the synchrotron data are smaller than those for the conventional data" [37] is probably the consequence of both the lower temperature of the data collection and the very high intensity available with the synchrotron radiation.

Messerschmidt et al. [36] compared the $\rho(\mathbf{r})$-derived electrostatic properties from four different experimental setups at three temperatures between 15 and 100 K. Two data sets were collected with conventional Mo $K\alpha$ radiation under N_2 gas stream at $T = 100$ K on a SMART three-circle diffractometer with APEX CCD area detector and on an EXCALIBUR2 four-circle diffractometer with a SAPPHIRE CCD area detector, respectively. The third data set was measured with synchrotron radiation at $T = 15$ K (Huber four-circle diffractometer, closed-cycle Helium cryostat), while the fourth set was obtained at $T = 25$ K with a Huber four-circle diffractometer equipped with standard sealed-tube Mo $K\alpha$ radiation, a

Table 19.1 Comparison of electronic parameters (d_n) at different temperatures[a]

	100 K	135a K	170a K	205a K
100 K		2.9	4.7	9.5
135a K	3.3		2.8	7.7
170a K	5.4	3.1		7.9
205a K	11.0	9.1	8.7	

[a]The variance-covariance matrix entry in the top row is used. (Reproduced from Ref. [34] with kind permission of The American Chemical Society).

closed-cycle Helium cryostat and an APEX detector. Good agreement was found, on average, among all four settings in terms of both the topological and the electrostatic properties. However, some unexpected dissimilarities in the electrostatic potential from the EXCALIBUR2 data set were reported. These disparities were attributed to differences in the integration software, but their origin could not be clearly explained. In any case, it was concluded that "in general, the lowest possible temperature should be used for charge-density determinations of organic compounds to obtain the optimum I/σ ratios".

A recent paper by Oddershede and Larsen [34] examines systematically the extent of the deconvolution of the thermal motion from the static density as temperature is increased. The authors undertook a study of the EDD of naphtalene at $T = 100, 135, 170$ and 205 K. Because of an unexpected reaction between the original sample and its coating epoxy glue, only the 100 K data obtained from this sample were used in the subsequent analysis. The higher temperature data collections were all performed on a second sample, coated with baby oil, and were labeled as 135a K, 170a K and 205a K, respectively. The refined atomic multipole coefficients p from the various data sets were compared by calculating their distance d_n in parameter space as obtained at two different temperatures, T_1 and T_2:

$$d_n = \left[\frac{1}{n} (p_{T_1} - p_{T_2})^t V^{-1} (p_{T_1} - p_{T_2}) \right]^{1/2} \tag{19.3}$$

where n is the number of independent refined parameters and V is the variance-covariance matrix at either T_1 or T_2. If the differences between p_{T1} and p_{T2} were due to random errors only, d_n is expected to be close to 1. In Table 19.1 (Table 3 in the original paper) the values of d_n for all the possible parameter comparisons among the four reliable data collections are reported.

Note that the distance is lower when the variance-covariance matrix of the higher temperature is used, because the variances increase with increasing temperature. The authors recognize that "multipole populations exhibit some variation with temperature", but state that only the 205 K parameters disagree systematically from the rest. They conclude that "the deconvolution of the thermal motion from the electron density has been achieved for the data measured below 200 K". This conclusion appears somewhat arbitrary, because it is not clear which value of d_n is to be adopted as a benchmark for assessing an acceptable similarity of the electronic

parameters. In addition, this statement lacks evidence coming from measurements at very low T: if the trend shown in the Table would be maintained down to 70, 40 or 20 K, the threshold for satisfactory deconvolution might have to be lowered to perhaps 100 K. Anyhow, the authors verified that the main features of the static experimental $\rho(\mathbf{r})$ were virtually identical to those obtained by theoretical calculations.

As regards the inorganic substances, it is well known that for a given temperature the ADP's of heavier atoms are significantly smaller than those of light elements such as carbon, nitrogen, oxygen and, of course, hydrogen. So, when only heavy elements are present, the deconvolution problem should be easily faced and, at least in principle,[3] accurate EDD studies do not need to be performed at low T. It appears that for inorganic compounds systematic investigations of the extent of deconvolution as a function of T have not been performed, but several room temperature studies of the static $\rho(\mathbf{r})$ have been reported [39–43]. In these cases short-wavelength or synchrotron radiation was used to collect a significant number of accurate high-order reflections[4] [44, 45]. However, while the agreement between the topological properties coming from synchrotron data sets and those obtained by theoretical calculations is generally good, the "experimental bcp properties, generated with conventional low energy X-ray diffraction data for several rock forming minerals, were found overall to be in poorer agreement with the theoretical properties" [46].

The evident conclusion is that no single upper limit of T for accurate experimental EDD determinations can be set, even for a specific, restricted class of compounds. Rather, there is general consensus on the significant advantages resulting from performing single-crystal XRD experiments at T as low as possible, especially when synchrotron radiation is used. Clearly, the quality of experimental $\rho(\mathbf{r})$ depends not only on T, but on several other features of the experimental setup as well, such as, for example, the beam homogeneity or the performances of the detector, together with the data collection and reduction strategies. Therefore, although very low temperatures ($T < 50$ K) are to be preferred, EDD's obtained at higher temperatures are not necessarily of lower quality. It is certainly true that the precision of the EDD-derived properties is generally higher in experiments performed at lower T.

---

[3]In fact, this is not always possible because of the occurrence of other phenomena which are to be handled with great care, such as anisotropic X-ray absorption and extinction, atomic anharmonic motion, and so on. Moreover, because of the large number of electrons in inorganic materials, the valence density contributes significantly to the diffracted intensities even at higher $\sin\vartheta/\lambda$ (not so for organic substances). Accordingly, measures carried out at higher 2ϑ are needed to perform a satisfactory deconvolution.

[4]Some pioneering works devoted to the determination of the electron density distribution were performed in the past at room temperature on home diffractometers, and actually dealt with very few (<20) structure factor amplitudes [44] or needed the replacement of lowest-angle, highly-extinction-affected reflections by data from X-ray diffraction powder measurements [45].
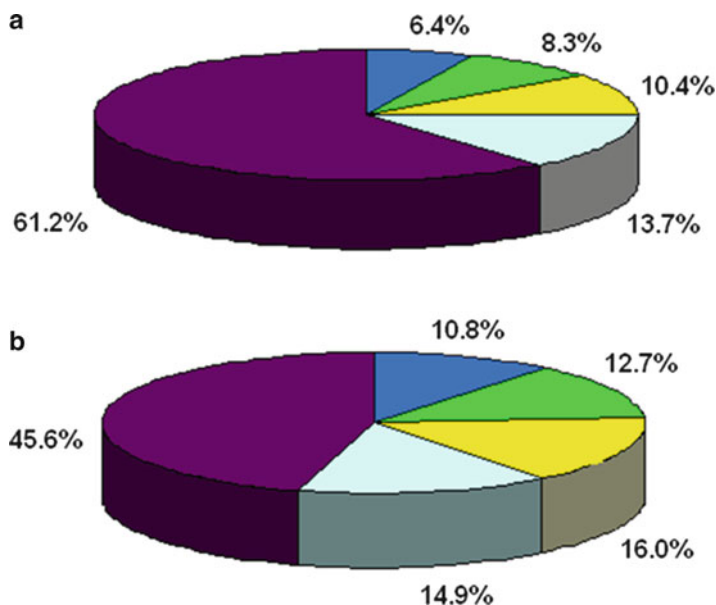
Fig. 19.2 Statistics of the measured intensities at (**a**) 23 K, (**b**) 115 K: ■ $I < 1\sigma(I)$; ■ $1\sigma(I) < I < 3\sigma(I)$; ■ $3\sigma(I) < I < 6\sigma(I)$; ■ $6\sigma(I) < I < 10\sigma(I)$; ■ $I > 10\sigma(I)$

19.2.4 Going Beyond the Convolution Problem: Comparison Between the Charge Density Distributions at $T = 23$ and 115 K from a Crystal of L-Alanine

All the works discussed so far are lacking a quantitative estimate of the gain in accuracy and precision for the electronic parameters when XRD experiments are performed at very low T. We obtained such an estimate in a test case, the aminoacid L-alanine, for which we collected high-resolution data of comparable quality, from the same crystal, at $T = 115$ K (hereinafter IT) and $T = 23$ K (LT). Full details of the LT crystal structure and charge density analysis, based on a slightly different data set, have already been reported [47–49].

As the temperature is lowered from 115 to 23 K, the number of very significant diffracted intensities ($I/\sigma(I) > 10$) increases from ∼50 to ∼61% (Fig. 19.2) and the number of very weak measures ($I < \sigma(I)$) decrease from ∼11 to ∼6%. Similarly, the number of unobserved data ($I < 0$) at 23 K is 1/3 of the corresponding quantity at 115 K.

A comparison of the electron population parameters (C_{plm}'s) obtained at the end of the multipole refinement (based on the Stewart formalism [21]) shows that, on average, the esd's of the C_{plm}'s for the LT are ∼0.7 times those at 115 K. The C_{plm}'s at the two temperatures are very similar, with an average difference of about 1 pooled esd (hereinafter σ_p); the largest deviation in terms of σ_p between the two
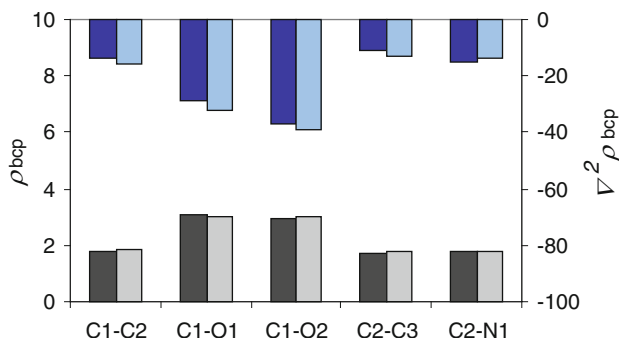
Fig. 19.3 Electron density and Laplacian at the bcp's. The *lower bars* show $\rho(\mathbf{r})$ values at the bcp's (*dark gray* for LT set and *light gray* for IT set), while the *upper bars* display $\nabla^2\rho(\mathbf{r})$ values at the same bcp's (*dark blue* for LT and *light blue* for IT)

sets is 3.7, and is observed for the monopole population of a hydrogen atom of the –CH$_3$ group.

As for the QTAIM properties of the experimental EDD, the LT esd's are again smaller than the IT esd's by a factor of $\sim$0.7. The topological properties at the two temperatures are very similar (see Fig. 19.3). The largest deviation between EDD values at the bcp (ρ_{bcp}) of the C–C, C–O and C–N bonds is 1.6 σ_p for the C1–C2 bond, and the average difference is 1.0 σ_p. Almost identical deviations are observed for the EDD Laplacian at the bcp ($\nabla^2\rho_{bcp}$). For the two C–O bonds, whose lengths differ by $\sim$0.02 Å [47, 49], it is found that the LT ρ_{bcp} value of the C1–O2 bond is smaller by 2.2 σ_p than the ρ_{bcp} value of the shorter C1–O1 bond, while the corresponding difference at IT amounts to 0.5 σ_p only. This suggests that, thanks to the correspondingly lower esd's, the LT data allow a finer discrimination between the chemical features of the two carboxylic oxygen atoms.

Figure 19.4 shows the experimentally derived molecular electrostatic potential $\Phi(\mathbf{r})$ from both data sets, mapped with the program MolIso [50] onto the isodensity surfaces of 0.00675 e Å^{-3}. The overall features of $\Phi(\mathbf{r})$ are largely comparable, and both maps exhibit a large charge separation, as expected. The minima of $\Phi(\mathbf{r})$ are equal within 1 esd, amounting to −464(49) kJ mol^{-1} and −486(72) kJ mol^{-1} for the LT and IT data set, respectively. The O2 atom is closest to the minimum in both cases (at distances of 1.148 and 1.159 Å, respectively). Although these findings suggest that the study of the molecular electrostatic potential does not require temperatures as low as 23 K, the esd's for this extensive property are significantly smaller at 23 K, making the experimental estimate of $\Phi(\mathbf{r})$ more reliable at 23 than at 115 K.

The IT and LT integrated QTAIM properties are also markedly similar. The largest and average differences between the QTAIM volumes of the four atom groupings in the alanine zwitterion (COO$^-$, NH$_3$$^+$, CH and CH$_3$) amount to 1 and 0.4 Å^3, respectively. The similarity is even more pronounced if the QTAIM group charges are taken into account: LT and IT estimates never differ by more than 1σ_{23K}.

Fig. 19.4 Molecular
electrostatic potential mapped
on the isodensity surface of
$0.00675\,e\text{Å}^{-3}$ for the alanine
molecule in the crystal. (**a**)
LT and (**b**) IT. The colour
scheme ranges from *red*
(negative) *via green* (neutral)
to *blue* (positive) with values
in the range $-410 \rightarrow +456$
$kJmol^{-1}$
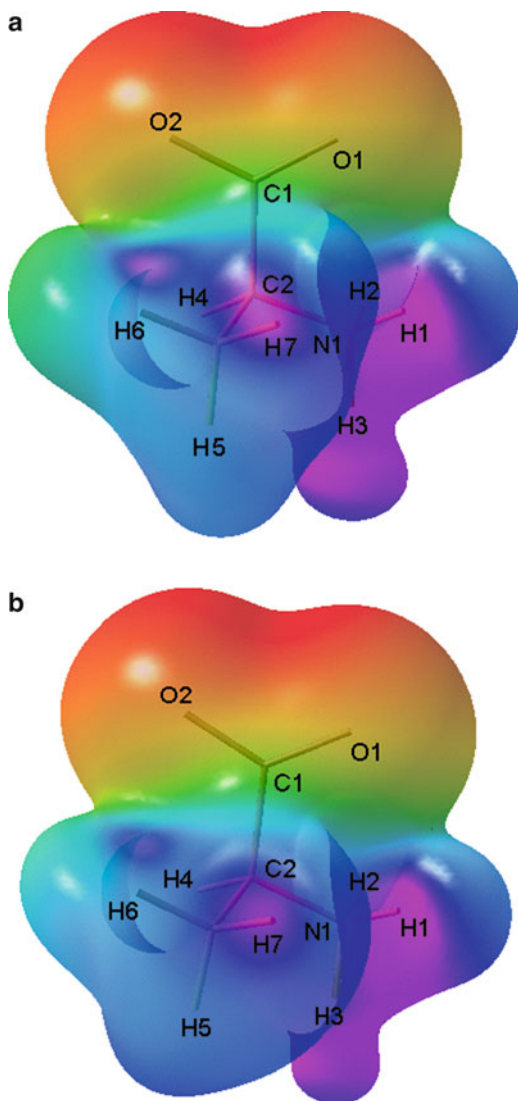
The dipole moments of L-alanine, based on QTAIM partitioning of the LT and
IT experimental EDD's, are listed in Table 19.2; all components are expressed in
the inertial reference system of coordinates. The following features can be noted:
(i) the values from the LT data set are slightly but systematically more precise than
those obtained from the IT set; (ii) the difference between the magnitudes of $\boldsymbol{\mu}$ for
the in-crystal estimates is larger than for the extracted molecule, but the difference
of 0.7 D is scarcely significant in terms of standard deviation; (iii) the polarization
of the electron density appears slightly more pronounced from the IT data; (iv) the

Table 19.2 Experimental molecular dipole moment (μ, Debye) from QTAIM partitioning of the EDD in zwitterionic L-alanine. First row: in-crystal values; second row: values for molecules extracted from the crystal, based on a cutoff of $\rho = 0.001$ atomic units (au)

	LT	IT
$|\mu|$	12.4(4)	13.1(5)
	12.1(4)	12.5(5)
μ_x	−12.2(4)	−12.9(5)
	−12.0(4)	−12.3(5)
μ_y	2.0(4)	1.8(4)
	1.9(3)	2.1(5)
μ_z	0.9(2)	1.5(2)
	0.9(2)	1.1(2)

Fig. 19.5 Linear correlation between experimental QTAIM values of the components of the in-crystal second moment (in debye Å) of the LT and IT data sets. The s.u.'s are reported as vertical/horizontal bars
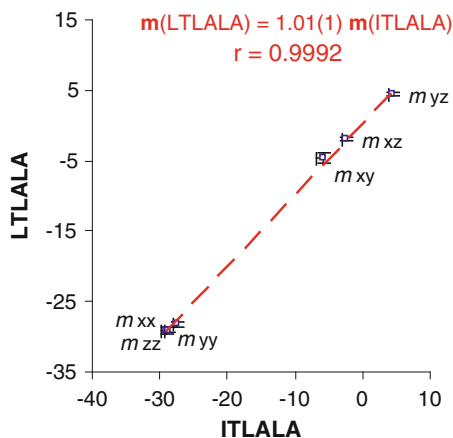
direction of the in-crystal dipole moment is in both cases roughly parallel to the principal axis of the molecule and to the **c** axis of the crystal, the angle between the latter and the dipole vector amounting to 1.0 and 0.1° for the LT and IT data set, respectively.

Individual components of the molecular second moments are graphically correlated in Fig. 19.5. The linear correlation between the experimental in-crystal QTAIM values from the IT and LT sets shows a slope of 1.01(1), indicating quantitative agreement between the values of the tensor components at the two temperatures.

Experimental estimates of the electrostatic interaction energy, E_{es}, for the three hydrogen-bonded molecular pairs in the aminoacid crystal at the two temperatures are summarized in the fourth column of Table 19.3 [see Fig. 4 of Ref. [49] for a graphical display of the three pairs A, B and C]. The values of E_{es} were obtained from the multipolar X-ray $\rho(\mathbf{r})$'s through the highly accurate EP/MM method [52, 53].

Within experimental error, the two data sets predict the same values of the electrostatic interaction energies, but again we find that the estimates from the IT data set are less precise than those obtained from the 23 K data.

This test case shows that the difference between the results obtained at the two temperatures is very modest, but the comparison proves that working at

Table 19.3 Electrostatic contribution (E_{es}, kJ mol^{-1}) to the total interaction energies for the three hydrogen-bonded molecular pairs of L-alanine

Pair[a]	Data set	d_{CM} (Å)[b]	E_{es}[c]
A	LT	5.7939	−149(10)
	IT	5.7913	−153(17)
B	LT	4.1541	−170(9)
	IT	4.1600	−184(12)
C	LT	5.1401	−25(4)
	IT	5.1360	−24(6)

[a]Symmetry operations relating the second molecule of a pair to the parent one (at x, y, z) are: A (x, y, −1 + z); B (1/2 + x, 1/2 − y, 1 − z); C (3/2 − x, −y, −1/2 + z)
[b]Distance between centres of mass of the molecules in a pair
[c]Obtained from the experimental $\rho(\mathbf{r})$ adopting the EP/MM method as implemented in the PAMoC code [51]. The esd's of the MM term are in parentheses

really low temperature ($T < 30$ K) increases the precision of the EDD and its derived properties. This is particularly important when studying intermolecular or interatomic low-density regions (e.g. metal-metal interactions in polynuclear coordination complexes), where it is crucial to assess the physical significance of subtle, very flat EDD features.

19.3 Interplay Between Electron Density and *T*-Driven Changes in Physicochemical Properties

In recent decades, exceptionally fast and accurate XRD data collections have become feasible at synchrotron facilities and home diffractometers equipped with very sensitive area detectors even for microcrystalline samples. Meanwhile, the increasing power of modern computers and the development of robust and fast algorithms for periodic calculations have made available various software packages [11, 12, 54] for accurate simulation of various physical properties in the solid state, such as magnetic coupling constants, optical properties, electronic structure, and so on. These developments facilitated correlation of the *T*-driven changes in such properties (either measured or theoretically estimated) with EDD, and elucidation of the interplay between lattice, electronic and magnetic degrees of freedom within the material. Nowadays, this field of study is of increasing importance and hopefully it will disclose in the next future new perspectives in crystal engineering and in the search for advanced materials. In the literature, two different approaches are followed to merge the information on EDD with that on other properties: in one approach, $\rho(\mathbf{r})$ is determined only at very low *T* by single-crystal XRD to provide insight into the physicochemical nature of *intramolecular* covalent or coordinative

interactions [55, 56]. In a second approach, the changes in the *intermolecular* $\rho(\mathbf{r})$ are examined as a function of T and, if necessary, they are correlated with the corresponding changes of other electronic or structural parameters [57, 58]. In the following discussion, two examples based on the latter approach will be presented.

The mutual interplay between crystal structure, $\rho(\mathbf{r})$, electron configuration and thermal motion was studied for the Kondo material CeB_6 [57]. The experimental EDD was obtained at four temperatures between 100 and 298 K and investigated using a non-conventional atomic orbital analysis [59, 60]. In particular, it was found that the lowering of T forces a charge transfer of $4f$ electrons from Ce to the B–B bonds connecting the B_6 octahedra, resulting in a significant enhancement of the anharmonic motion of the metal ion. Enhanced anharmonicity raises the entropy and provides the driving force for the electron transfer. The authors claim that "changes in crystal structure, electron density, electron configuration and anharmonic vibration are found to be closely correlated with one another". Eventually, they conclude that "multidimensional X-ray diffraction analysis in which temperature, time and energy are added as experimental variables to the three dimensions of space will be a very fascinating field in science".

A recent study follows the strengthening of intermolecular interactions in pentaerythritol and corresponding changes in the intermolecular electron density, both due to a lowering of temperature or to an increase of pressure [58]. This substance forms hydrogen-bonded layers, which come closer at low T or high p. At the same time, the intermolecular interaction energies become more negative, while topological and energetic indicators at the bcp's of $\rho(\mathbf{r})$ signal the enhancement of the interlayer attractive interactions. On the other hand, the interactions within each molecular layer are found to become weaker on the same grounds. As a take-home message it can be learned from this work that it is possible to *quantitatively* relate changes in charge density within the unit cell with changes in the *observed* crystal packing as a function of T (or p).

As pointed out in the introduction of this chapter, a lowering of T may sometimes induce significant conformational and packing rearrangements of the asymmetric unit, i.e. structural phase transitions may occur. If an accurate $\rho(\mathbf{r})$ is available (experimentally or theoretically) both above and below the transition temperature T_{tr}, structural phase transitions can be characterized quantitatively in terms of the observed changes in intermolecular (or atom-atom) interactions, energetics, and electrostatic moments, thus providing insight into the mechanism[5] of the phase transition. The next Sections deal with this topic, showing a few examples of single-crystal-to-single-crystal phase transitions induced by a change in temperature and studied from the EDD point of view.

---

[5]In the literature, the mechanism of solid-solid phase transitions is usually associated to thermodynamics or structural considerations rather than kinetics, which would imply the knowledge of nucleation and growth dynamics of the new phase in the bulk. Accordingly, hereinafter the term "mechanism" is intended in the pure applicative meaning of "way by which atoms displace across the transition".

19.3.1   Electron Density Analysis Across Structural Phase Transitions: The Case of Organic Charge-Transfer Complexes

So far only a few studies have been devoted to the characterization of structural phase transitions through EDD analysis, probably because the requirements for an accurate determination of the experimental $\rho(\mathbf{r})$ are very demanding. Organic charge-transfer complexes are the most studied substances from this point of view. These materials are composed of flat molecules, which invariably pile up in parallel stacks. Since the 1970s they attracted great interest as low-dimensional electric conductors. Their electronic properties are heavily T-dependent, and the detailed knowledge of the changes in intermolecular interactions at the atomic level (hence of the EDD) in a wide T range is mandatory to explain their transport properties exhaustively. The literature concerning this topic is very rich, but we refer here to those studies which are explicitly aimed at the experimental and/or theoretical $\rho(\mathbf{r})$ analysis above and below T_{tr}.

A first example is the charge-transfer complex anthracene-tectracyanobenzene (A–TCNB), which undergoes a single-crystal-to-single-crystal second-order, order-disorder phase transition at $T_{tr} = 206$ K. This system was studied in great detail during the 1980s by means of both experimental and theoretical techniques; the disordered phase above T_{tr} was interpreted as "dynamically disordered" in an early EDD study performed in 1980 [61]. The paper reports the experimental EDD for both the molecules in the complex, obtained at seven different temperatures above and below T_{tr}. The high-T and low-T phases were assigned to the space groups Cm and P2$_1$/a, respectively. In Fig. 19.6, an excerpt of Fig. 1 in Ref. [61] is reported, showing the EDD plots of anthracene obtained as direct Fourier summations over the observed structure factors amplitudes F$_o$'s. The large, smeared contours in $\rho(\mathbf{r})$ around the C4–C4M and C7–C7M bonds of anthracene above T_{tr}, mirrored by equally large and elongated thermal ellipsoids on the atoms C4, C4M, C7 and C7M were originally interpreted as the effect of librational motion around the normal to the molecular plane, i.e. as a sign of dynamic disorder. These findings were heavily criticized in a later work [62], which proposed the symmetry C2/m as a valuable alternative for the high-T phase. A static model for the disordered anthracene was also proposed, in which anomalous, large thermal ellipsoids arise because of the superposition of two molecules, inclined at $\pm 6°$ with respect to the mirror plane in Cm. Subsequent works [63–65] maintained the C2/m symmetry for the high-T phase, but at the same time confirmed that the orientational disorder of anthracene is better described as dynamic, in agreement with the original proposal [61]. As pointed out by Larsen [15], "sometimes it is difficult to disentangle in a crystallographic study the results of molecular disorder", and "data collected at different temperatures may be of help in obtaining structural information by discerning between statistical and dynamic disorder".

The tetrathiofulvalene–chloranil complex (TTF–CA) is a key example of a T-driven neutral-ionic phase transition of the first-order [66]. It takes place at
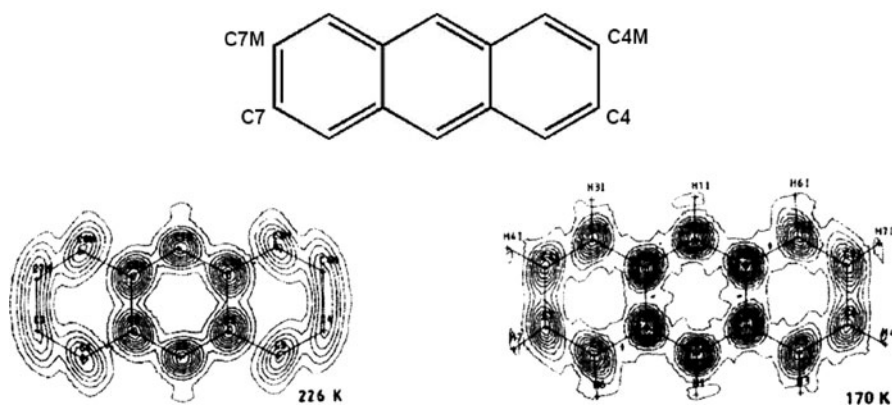
Fig. 19.6 Excerpt of Fig. 1 of Ref. [61]. Electron density, F_o, plots for the A molecules of A: TCNB at the indicated temperatures. The picture at left contains examples of the high-T phase; that at right displays examples from the low-T phase. Plots are contoured at 1e $Å^{-3}$ levels (Reproduced from Ref. [61] with kind permission of The American Institute of Physics)

$T_{tr} = 81$ K, involving a reduction of the crystal symmetry from P2$_1$/n (high-T phase) to Pn (low-T phase) and abrupt changes in the amount of charge transfer, optical and transport properties. The EDD of this complex [67], especially the corresponding QTAIM descriptors, was studied theoretically as a function of T using plane-wave calculations based on experimental neutron-diffraction geometries obtained at $T = 40$, 90 and 300 K. A direct relationship was found between the relative variations of the potential energy density at the intermolecular bcp's and the intermolecular distances. The lowering of T causes an increase in the strength of all the intermolecular interactions; shorter contacts are strengthened more, on average, than the longer ones. Moreover, the amount of the charge transfer was studied as a function of T both topologically and with other methods; results were found to be in close agreement with each other and indicated a charge transfer of about 0.45 e at 300 K and 0.65 e at 40 K, occurring from TTF (donor) to CA (acceptor). The combination of an EDD study with electronic structure calculations gives a valuable insight into the transition mechanism. The authors claim that their "results on TTF-CA show that HOMO-LUMO overlap and hydrogen bonds dominate the intermolecular interactions in both high- and low-temperature structures and drive the molecular deformation and reorientation occurring" at the neutral-ionic transition.

More recently, high-resolution single-crystal XRD experiments on the same system, both above ($T = 105$ K) and below ($T = 15$ K) T_{tr}, were performed to accurately characterize the intra- and interstack intermolecular interactions and the amount of charge transfer directly from the experiment [68]. In particular, the charge transfer q_{CT} was related to the observed changes in the intermolecular interactions and in the covalent bond lengths of the TTF and CA molecules. The amount of q_{CT}, estimated through the integration of the observed $\rho(\mathbf{r})$ inside each atomic basin,

was found to be as large as 0.21 (2) e at 105 K and 0.77 (2) e at 15 K. On going from 105 to 15 K, the TTF C=C bond lengths increase, whereas the lengths of the C–S bonds decrease (although the latter shortening is barely significant in terms of the experimental esd's). In CA, on the other hand, the single C–C bond distances decrease, while the C=C, C=O and C–Cl distances increase. These findings were rationalized in terms of the charge transfer from the TTF HOMO into the CA LUMO, the latter being π antibonding for both C=O and C–Cl bonds. It should be noted, however, that these conclusions assume that the thermal motion has been properly deconvoluted at both temperatures.

As regards the intermolecular interactions, the topological analysis of the experimental EDD both above and below T_{tr} showed that "the C–H$\cdots$O intrastack contacts are the strongest interactions and are reinforced in the low-T phase, whereas the strength of the Cl$\cdots$Cl interactions do not change across the transition". The authors claim that in the low-T phase "the creation of pairs of donor-acceptor dimers clearly shows up, with an increase of the intradimer charge density". The statement that the dimer "is clearly identified" by plotting the $\rho(\mathbf{r}) = 0.065$ e Å^{-3} isocontour in the unit cell, appears to be somewhat arbitrary. The authors conclude that "accurate X-ray measurement and electron density modelling is a necessary tool to directly investigate intermolecular interactions and tiny charge transfers" and acknowledge that "agreement between theory and experiment is not fully satisfactory and requires more accurate calculations and modelling". Indeed, plane wave theoretical DFT calculations are not able to reproduce the observed charge transfer across the transition and disagree in the position of some intermolecular cp's with respect to the experimental results.

Another theoretical study on a similar complex, 2,6-dimethyltetrathiofulvalene-p-chloranil (DMTTF–CA), was recently performed [69], and led to substantially similar conclusions.

19.3.2 Tracking the Temperature Dependence of the EDD Topology Near a Phase Transition: The Case of KMnF$_3$

Several interesting physical properties of perovskite-type inorganic materials, such as piezoelectricity, dielectric susceptibility, and magneto-transport properties, are related to distortions from the ideal, cubic structure with P m$\bar{3}$m symmetry. The perovskite KMnF$_3$, for example, undergoes a weak first-order phase transition, in which the room temperature cubic phase is tetragonally distorted (I4/mcm) below $T_{tr} = 186$ K. The transition involves the alternate rotation of the MnF$_6$ octahedra about the C$_4$ cubic axes. Ivanov et al. [70] have performed single-crystal XRD experiments at 190, 240 and 298 K with the aim of following the effect of T on the experimental EDD topology immediately preceding the phase transition. In this study, important experimental requirements have been fulfilled: the sample was grown to a sphere, the reciprocal lattice was explored up to very high resolution

to account for anharmonic thermal displacements, and absorption and secondary extinction corrections were properly considered. Therefore, the obtained results appear very reliable in terms of accuracy, although the reported λ_1 and λ_2 curvatures (see Table 3 in Ref. [70]), which are very close to zero and scarcely significant in terms of esd's, may cast some doubts on the critical points classification. The authors demonstrated that the chemical bonding network started to adjust 50–60°C above T_{tr}. At 298 K only cation–anion (Mn–F and K–F) bond paths are evident, with a cage critical point lying on the C_3 axis along the Mn–K vector (Fig. 19.7). As T is lowered, the cage critical point disappears and the ring critical point (rcp) on the (110) plane moves towards the threefold axis; at the same time, a new Mn–K bcp appears in the neighbourhood of the rcp. At $T = 240$ K these two points are only 0.04 Å apart, i.e. the system is close to a topological catastrophe according to Bader's QTAIM [3] (Fig. 19.7). When the temperature is lowered further (Fig. 19.7), the bcp and the rcp veer away from each other (at $T = 190$ K they are 0.35 Å apart) and the topological indicators of the Mn–K interaction clearly indicate its strengthening. At the same time, the K–F interaction becomes weaker. The authors interpreted their findings as a precursor effect, i.e. as a reconstruction of the bonding network of the system as it approaches the phase transition temperature. It is worth noting that, although in this study the EDD was not obtained both above and below $T_{tr,}$ its detailed topological analysis as a function of T provided insight at atomic resolution into the bonds rearrangement near the phase transition itself.

19.3.3   The Elusive Phase Transition of the Fungal Metabolite Austdiol Below 70 K

Sometimes, the occurrence of structural phase transitions can be revealed indirectly from low-T EDD studies, as illustrated by the following example.

Austdiol ($C_{12}H_{12}O_5$, $P2_12_12$, $Z = 4$ [71]; see Fig. 19.8 for the molecular formula and the atom numbering scheme) is the main toxic component of a mixture of substances produced in mouldy maize meal by the fungus *Aspergillus Ustus*. A single-crystal XRD data collection aimed at the accurate determination of the EDD was performed at very low T (20 K) several years ago. Intensities, profile shapes (at azimuthal angle $\Psi = 0$), redundancy and resolution of both data sets seemed of satisfactory quality for an electron density study. Although at first glance there was no evidence of a structural transformation (e.g. cell distortions, changes in the systematic extinction rules, appearance of satellite peaks, and so on), the ADP's of the heavy atoms looked very anomalous at the end of the spherical atom refinement (Fig. 19.8). All the ellipsoids were elongated in the same direction, almost parallel to the **b** axis (which is the longest one). These unexpected features did not depend on the $\sin\vartheta/\lambda$ cutoff adopted in the refinement, i.e. both the high-order and the low-order reflections led to the same, clearly unphysical, ADP shapes. At room temperature, the thermal ellipsoids assumed a normal shape, with U_{ij} values identical to those determined at the same T before the low-T data collections.
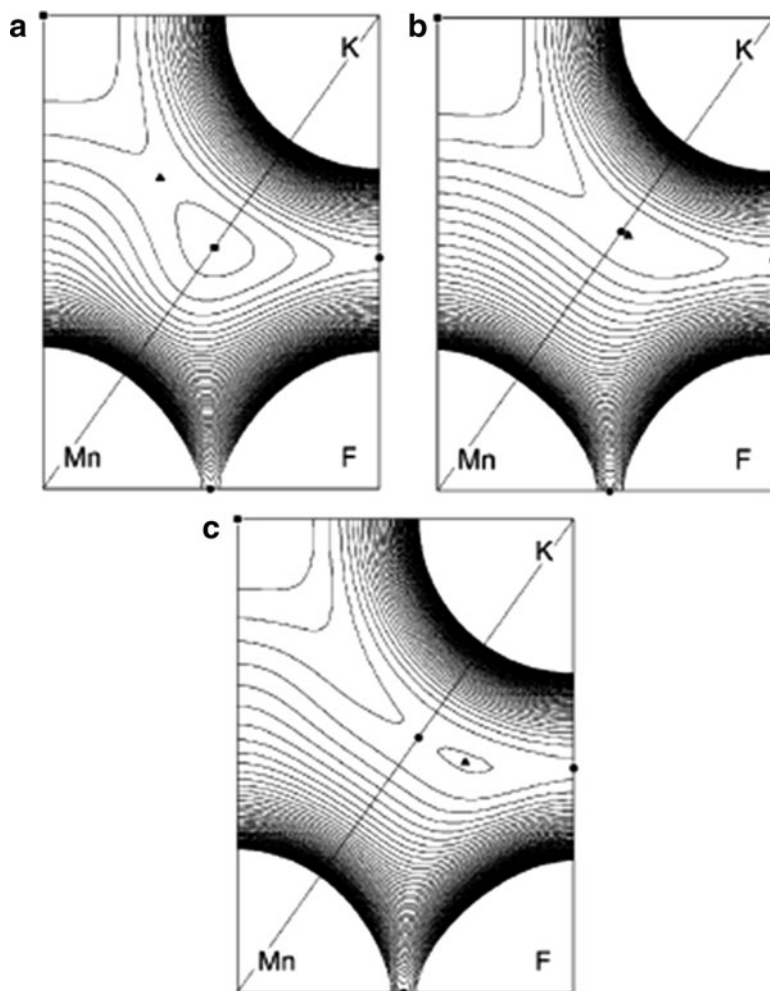
Fig. 19.7 Static model of the total electron density in the (110) plane of $KMnF_3$ at (**a**) 298, (**b**) 240 and (**c**) 190 K. Contour interval: 0.01 e·Å^{-3}. The critical points of the electron density are denoted as follows: filled circles: (3,–1), bond; filled triangles: (3,+1), ring; filled square: (3,+3), cage (Reproduced from Ref. [70] with kind permission of the International Union of Crystallography)

An accurate multi-temperature study was then carried out on several samples of austdiol, crystallized from various solvents, to understand the origin of the observed anomaly in the molecular thermal motion. Eventually, it was concluded that it was due to some kind of fully reversible structural transformation affecting the observed diffraction intensities below $T = 70$ K. Indeed, several azimuthal scans, performed at $T = 62$–64 K on intense, low-order reflections, showed a clear splitting of the profiles when the azimuthal angle Ψ was different from zero (Fig. 19.9); the same
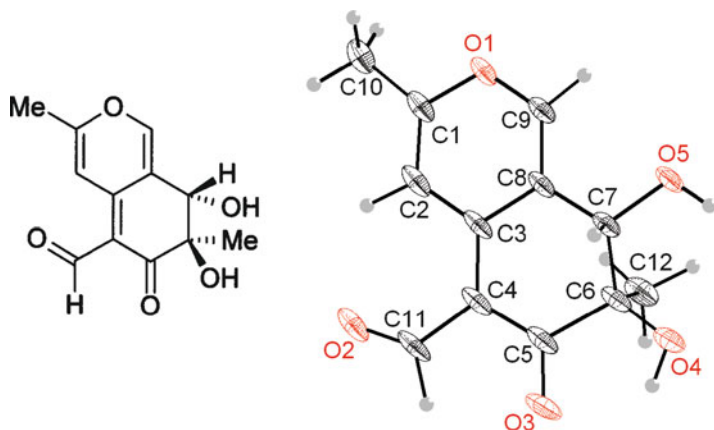
Fig. 19.8 Austdiol ($C_{12}H_{12}O_5$): molecular formula and connectivity, with the atom numbering scheme, as obtained from the single-crystal X-ray diffraction experiment at $T = 20$ K (see text). The thermal ellipsoids are drawn at the 75% probability level. The ball-and-stick picture was realized with the Diamond v3.2a graphical software, © Klaus Brandenburg (1997–2009) Crystal Impact GbR, Bonn, Germany
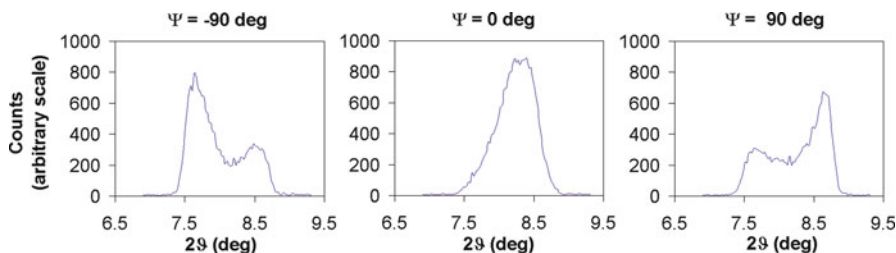

Fig. 19.9 Azimuthal scans for the $-1\ 0\ 1$ reflections of austdiol at $T = 62$ K

profiles appeared perfectly normal in shape when the azimuthal scan was performed at room temperature. Having determined $T \sim 64$ K as the possible temperature for the beginning of the phase transformation, the accurate EDD study was based on data measured at slightly higher temperature, i.e. at $T = 70$ K [72].

This test case shows that it is necessary to verify the accuracy of an EDD analysis not only in terms of local EDD descriptors, especially when anomalous ADP's, or surprising changes in electrostatic moments, are found. In fact, this kind of unusual findings is likely to be the consequence of an inadequate multipole model and/or of wrong data treatment [73] or, as in this case, they may signal an unexpected and otherwise elusive structural transformation.

19.4 Charge Density Studies of Temperature-Dependent Phenomena: Spin-Crossover and Associated Changes in $\rho(\mathbf{r})$

19.4.1 Introduction

As stated at the beginning of this chapter, changes in temperature may not only have a direct effect on atomic positions, and hence on molecular and crystal structure, but may also alter the features of the electron density distribution $\rho(\mathbf{r})$ by inducing changes in the population of certain atomic orbitals. Spin crossover (SCO) in transition metal complexes is a typical example of this.

When a transition metal ion is subject to a ligand field the degeneracy of the five atomic d-orbitals is broken and different spin states become possible. The final spin state of the metal will depend on the energies and populations of the non-degenerate d-orbitals. In the frequent case of an octahedral ligand field, the *lobes* of the $d_z{}^2$ and $d_x{}^2{}_{-y}{}^2$ orbitals are oriented along metal-ligand axes, leading to an increase in their energy due to repulsion from the electrons in the ligand orbitals. By contrast, it is the *nodes* of the d_{xy}, d_{xz} and d_{yz} orbitals that lie along the metal-ligand axes, resulting in a decrease in energy of these orbitals. The difference in energy (Δ) between the destabilised orbitals (the e_g set) and the stabilised ones (the t_{2g} set) depends on the nature of the bonded ligands. Spin-pairing two electrons in the same orbital requires a pairing energy (P). The relative magnitude of Δ and P governs the electron distribution within the orbitals (Fig. 19.10). If $\Delta < P$ then Hund's Rule is obeyed, i.e. all five d-orbitals will be singly occupied prior to spin-pairing of electrons in the t_{2g} set; maximum spin multiplicity is achieved. This case is referred to as high-spin (HS). Conversely, when $\Delta > P$, the orbital occupation is governed by the Aufbau Principle, allowing for full occupation of the t_{2g} set prior to population of the e_g set; spin multiplicity is at a minimum. This case is then referred to as low-spin (LS). The spin state of a metal ion can then be controlled through a modification of the ligands around the metal, i.e. through a change in the ligand field strength. With appropriately chosen ligands, the spin crossover phenomenon can be observed: an intra-ionic electron transfer between the e_g and t_{2g} orbitals producing a change in the spin state. This is usually induced by a perturbation to the sample environment, such as a change in pressure or as a result of light irradiation. However, the most common stimulus to induce this effect is a change in temperature, the low spin state being inherently more stable at low temperatures and the high spin state being the more stable at higher temperatures. Although SCO is markedly more common in d^6 iron(II) complexes, it is also possible in any transition metal that has an electronic configuration between d^4 and d^7.

HS and LS configurations are structurally and electronically very different and can easily be distinguished from the metal-ligand bond distances: population of the anti-bonding e_g orbitals and depopulation of the non-bonding t_{2g} orbitals will lengthen them, as has been observed numerous times [74]. Accompanying
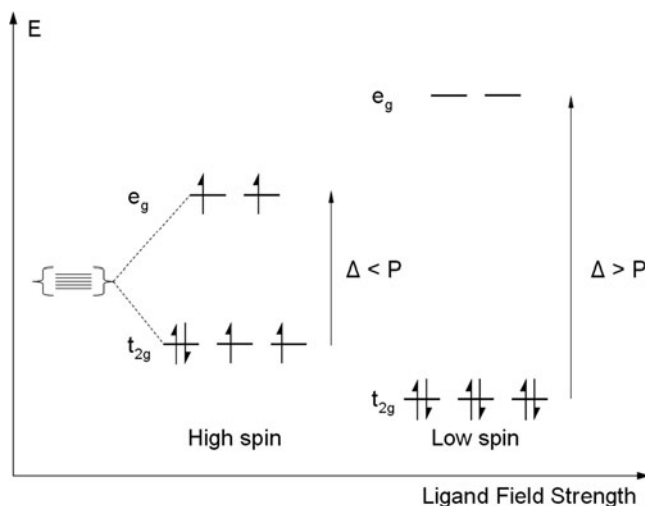
Fig. 19.10 Schematic representation of the electronic configuration of a d^6 metal ion in an octahedral ligand field, in the HS and LS states

differences in the electron density distribution have not been studied as extensively, but have been analysed on the basis of high resolution diffraction data for some materials in either the LS or the HS state, in particular for porphyrins and phthalocyanines [75–80]. As in the case of a structural phase transition, obtaining the experimental $\rho(\mathbf{r})$ above and below a spin transition would improve our understanding of the relationship between the changes in the electronic and molecular structure, by relating them to the changes of the scalar field $\rho(\mathbf{r})$ itself.

However, performing such an experiment would introduce additional effects inherent to the temperature difference. This difficulty can be circumvected by making use of the thermal hysteresis frequently present in these systems. This would allow to obtain $\rho(\mathbf{r})$ for the HS as well as the LS states of a complex at the same temperature. The challenge here is to find a suitable sample, one that does not introduce other intrinsic difficulties, such as the presence of another heavy metal. The material must also form high quality crystals and present a transition with a wide hysteresis loop centered at a temperature low enough to allow this kind of study. To our knowledge, no such high resolution diffraction study has been published to date. Milen & Maslen published in 1988 electron density studies at 295 K and 120 K of an iron(III) spin crossover complex showing a gradual transition centred at ~200 K [81]. Much more recently Pillet et al. [82] reported electron density studies of the light induced metastable high spin state of $Fe(phen)_2(NCS)_2$. However, the work reported by Legrand et al. [83] on the electron density studies at 15 K of the LS and quenched HS states of $Fe(btr)_2(NCS)_2 \cdot H_2O$, comes closest to the scenario mentioned above.

19.4.2   *Charge Density Analysis of Fe(btr)$_2$(NCS)$_2$·H$_2$O*

The compound Fe(btr)$_2$(NCS)$_2$·H$_2$O (btr: 4,4'-bis-1,2,4-triazole) undergoes an abrupt, complete spin transition with a hysteresis width of 21 K (T$_{1/2\downarrow}$ = 123.5 K, T$_{1/2\uparrow}$ = 144.5 K) as revealed by magnetic susceptibility and Mössbauer spectroscopy measurements [84]. Initial structural information on this compound was reported at room temperature [84], however, Pillet et al. carried out a careful structural study of the thermal HS-LS transition, showing that it occurs through a domain nucleation and growth process [85]. The crystal structure shows layers parallel to the *bc* plane, formed by each Fe(II) centre coordinating to the terminal N-atoms of 4 btr ligands in the basal plane. The octahedral coordination of each Fe(II) is completed by two NCS groups in *trans* position, predominantly aligned along the *a*-axis.

An electron density distribution study on this compound, both in the LS and HS state, was reported by Legrand et al. [83]. The results reported are not from data collected at a temperature within the hysteresis loop, which is too high to allow proper deconvolution of the thermal smearing effects from the deformation density. However, the authors collected high quality data of the LS and quenched HS states at 15 K. Thermal quenching was achieved by flash freezing the crystal in a cold stream of He gas. This procedure allowed comparison of the electron density in different electronic states at the same temperature. Differences in the atomic displacement parameters are then likely to only represent the modification of vibrational modes and amplitudes due to the structural changes induced by the spin transition.

The quenched HS state is a metastable state but relaxation of metastable HS states is, in general, very slow at temperatures below 30 K, in particular for highly cooperative systems. In this case, the rate of relaxation was slow enough to allow collection of high resolution diffraction data from the quenched HS state sample and hence, obtain a full characterisation of this state by the analysis of the electron density distribution.

The static deformation densities in the mean plane of the triazole ring in both the HS and LS states show characteristics similar to those observed in a study of a btr crystal [86]. In fact, identical deformation density features are observed for both spin states with the exception that, in the HS state, there is a displacement of density towards the metal-coordinated nitrogen of the triazole's N–N bond.

As expected, the electron density around the metal centre shows very different features depending on the spin state (Fig. 19.11). In the LS state, negative deformation density is found in all six Fe-N coordination bonds; this is interpreted as a depopulation of the d$_{x^2-y^2}$ and d$_{z^2}$ atomic orbitals with respect to the isolated Fe atom. Similarly, along the diagonal directions, corresponding to the d$_{xy}$, d$_{xz}$ and d$_{yz}$ atomic orbitals, positive deformation density can be observed. These features are in agreement with the aforementioned splitting of the Fe 3d orbitals into the e$_g$ and t$_{2g}$ energy levels, when the metal sits in an octahedral environment. Figure 19.11 shows that the nitrogen lone pairs of the btr and NCS groups are directed towards the Fe(II) ion, with a maximum of deformation density along the Fe-N axes. The
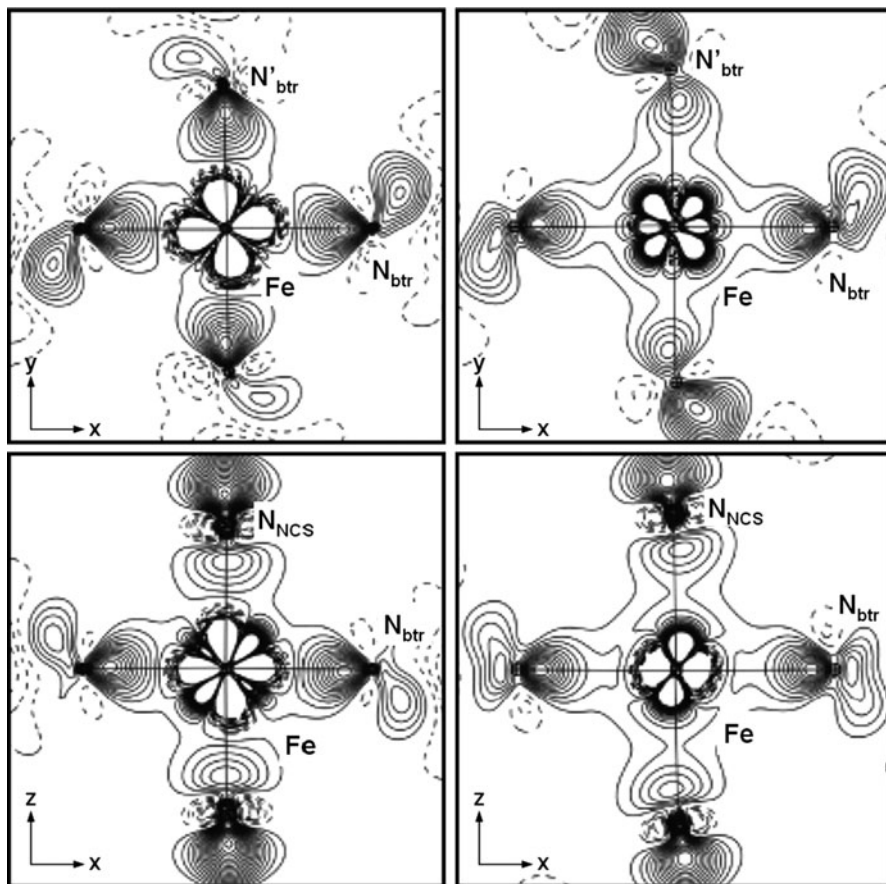
Fig. 19.11 Static deformation density in the triazole-Fe basal plane (*top*) and perpendicular to the basal plane (*bottom*) for the LS (*left*) and HS (*right*) states. Contour levels at 0.05 e/Å^3; positive contours shown as solid lines and negative as dashed lines (Adapted from [83] with kind permission of The American Chemical Society)

deformation density corresponding to the NCS nitrogen lone pair is smaller and more diffuse in directions perpendicular to the Fe-N axis compared to those of the btr nitrogen atoms. In general, the nitrogen deformation density extends to the Fe site, indicating a significant covalent character of the Fe-N bonds in the LS state.

In the HS state, some of the negative deformation density in the direction of the basal btr nitrogen atoms is retained. Positive deformation density is accumulated in the axial direction though, in contrast to the LS state (Fig. 19.11), indicating a large electron redistribution among the Fe 3d orbitals. As for the LS state, the deformation density corresponding to the lone pairs of the coordinating N-atoms extends towards the Fe site, indicating some covalent character of the considerably longer Fe-N bonds. The electron density features of the btr and NCS ligands are very

similar in both spin states, in agreement with the SCO effect being a charge transfer within the metal atom, hence no significant changes in the ligands are expected.

Multipolar electron density studies on transition metal complexes (or any other fitting of the charge distribution by analytical density functions) allow direct calculation of the 3d orbital populations [87]. This could not be more suitable than for the case of Fe(II) spin crossover complexes, where not only the differences in those populations is pronounced but also where they are so closely related to the magnetic properties. The relationships between populations of spherical harmonic functions on metal atoms and d–orbital occupancies have been derived within the limits of crystal field theory, which neglects covalent interactions between the metal atom and ligands [88]. Hence, orbital population calculations are most reliable when the metal and ligand orbitals do not strongly overlap. As discussed above this assumption is not strictly valid for the present compound as there may be significant covalent character present in the Fe-N bonds. However, the approximation has been proven to be sufficient when a moderate overlap is present [89] and it can clearly detect the differences between high and low spin states as well as small values of orbital occupancies ascribed to σ-donation and π-back-donation [75–80]. Hence, it is expected to also yield enlightening results for the present case.

A comparison of the orbital populations calculated from the multipolar model of the electron density, for the HS and LS states, with the Crystal Field theory ideal orbital populations for Fe(II) in an octahedral ligand field, are shown in Table 19.4. The populations calculated for the LS state agree well with those of a d^6-Fe(II) metal centre having all electrons in the t_{2g} orbitals and none in the e_g orbitals. Nonetheless, the crystal field destabilized $d_{x^2-y^2}$ and d_{z^2} orbitals exhibit some population, attributed mainly to σ-donation from the NCS and btr ligands due to a high metal-ligand σ overlap. Table 19.4 shows that the amount of electron donation from the ligands to the metal is the same, 0.1 e by each NCS group and 0.1 e by each triazole ring. In the (metastable) HS state, all 3d orbitals are more uniformly populated, consistent with theoretical predictions. Part of the differences in populations between experiment and theory in both the LS and HS states have been ascribed by the authors of this work to π back-bonding. However, another reason for the discrepancy can be the deviations from perfect octahedral symmetry: different ligands, M–N bond distances and N–M–N angles; the latter deviating from right angles. Hence, it can be expected that the theoretical orbital occupancies will not necessarily be those ideally predicted by crystal field theory. Even with differences much smaller than the ones observed in this case, the asphericity of the electron density around the metal resulted in noticeable changes in orbital populations for the case of $Cr(CO)_6$ [90]. Nevertheless, taking into account the errors associated with the diffraction data and the possible differences in expected theoretical values, the experimental results reflect the differences anticipated for LS and HS states as suggested by the theoretical predictions of crystal field theory.

Topological analysis of the charge distribution [3] has yielded values of the electron density at the Fe–N bond critical points (bcp's) that mirror the differences in bond distances, i.e. they are systematically higher in the LS state where shorter and stronger Fe–N bonds are observed. However, a better characterization of metal-

Table 19.4 Atomic orbital populations from experimental X-ray data on $Fe(btr)_2(NCS)_2 \cdot H_2O$ [83]

	d_{xy}	d_{xz}	d_{yz}	$d_{x^2-y^2}$	d_{z^2}	Total 3d population
LS	1.50	2.22	1.94	0.40	0.20	6.26
HS	1.59	0.94	1.17	0.95	1.49	6.14
LS (theo)	2	2	2	0	0	6
HS (theo)	1.33	1.33	1.33	1	1	6

(Reproduced from Ref. [83] with kind permission of The American Chemical Society)

ligand bonding may be given in terms of the kinetic $G(\mathbf{r})$ and potential $V(\mathbf{r})$ energy densities at the bcp's, where a larger degree of covalent character is associated with an excess of potential energy over the kinetic energy density. Both quantities can be obtained through the Abramov approximation [91]. In the present case, the potential energy density of the Fe-N bonds dominates the total energy density, while the normalised kinetic energy density $G(\mathbf{r})/\rho(\mathbf{r}) > 1$, indicating an intermediate type of bond [92], with some covalent character.

The Laplacian of the electron density indicates the location of local charge concentration ($\nabla^2\rho < 0$). In this case, the Laplacian distribution in the FeN_4 planes clearly shows minima close to the N atoms and towards the Fe ion, corresponding to the electron concentration of the N lone pairs. However, the Laplacian distribution around the Fe ion shows different features depending on the spin state. The authors of this work have found that in the LS state, isovalues of the Laplacian adopt a cubic shape with faces perpendicular to the Fe-N bonds. The actual values of the Laplacian show charge deficit along the bonds, i.e. on the faces of the cube, and concentration of charge as far as possible from these, i.e. on the vertices of the cube. Such a distribution is expected for octahedrally coordinated d^4–d^7 transition metals subject to a strong ligand field, such as an Fe(II) ion in the LS state, due to the electron density and lack of density associated to the t_{2g} and e_g orbitals respectively [93, 94]. In contrast, charge concentrations in the HS state are located along the z axis and along the diagonal directions of the basal plane, fully consistent with the 3d orbital populations described before.

The example summarized above shows that the experimental electron density distribution in a spin crossover complex is consistent with the predictions of ligand field theory, commonly used to explain the observed physical properties of these complexes, and with information obtained by other techniques.

19.4.3 Electron Density Rearrangements in Spin Crossover Systems

The features of the electron density above and below the SCO transition for the most commonly studied mononuclear pseudo-octahedral iron(II) SCO complexes

have been described in Sect. 19.4.2. However, there are other examples of SCO transitions that involve more considerable rearrangements of the electron density. Although no formal electron density distribution studies have been published to date on any of these systems, it is worth describing structural results from a few of these cases.

19.4.3.1   Spin Crossover Associated to a Reversible Change of Coordination Number

Given the intraionic nature of the spin crossover, the most important changes on the electron density due to such a transition are observed around the metal, although always keeping its coordination number. However, in 2007 Guionneau et al. reported thermal and light induced spin crossover transitions on $FeL(CN)_2 \cdot H_2O$ (L:2,13-dimethyl-6,9-dioxa-3,12,18-triazabicyclo[12.3.1]octadeca-1(18),2,12,14,16-penta-ene) [95]. The magnetic transitions on this complex are associated to a large modification of the electron density and bonding features around the metal, as the metal changes from 7-coordinate in the high spin state ($FeN_3O_2C_2$) to 6-coordinate (FeN_3OC_2) in the low spin state. The material undergoes a thermal spin transition between 250 K and 150 K, with different degrees of completeness, depending on the cooling rate. Above 250 K the structure is such that the iron(II) is in a pentagonal bipyramidal environment with the metal lying on a two-fold axis. The symmetry restricts the Fe-O distances to be the same. Below the transition, there is a loss of symmetry associated to a Fe–O bond breaking, since the Fe–O bond lengths of 2.334(1) Å at room temperature become 2.243(1) Å and 3.202(1) Å. It is obvious then the large degree of change in electron density distribution around the metal, involving the change of coordination from 7 to 6. In pseudo-octahedral iron(II) complexes, it has been shown that the volume of the coordination polyhedron decreases from 13.0(5) $Å^3$ in HS to 10.0(5) $Å^3$ in LS [96]. The drastic and large change in molecular structure in the present case, is also demonstrated by the volume of the coordination polyhedron around the metal decreasing from 17.0(1) $Å^3$ to 10.0(1) $Å^3$, more than double the standard case.

Another remarkable change of this complex molecular structure after the transition from HS to LS is the inversion of the $O–CH_2–CH_2–O$ ethylene ring conformation. This is shown for example by the distance ethylene carbon atoms to the mean plane defined by the two oxygen atoms and the metal. In the HS state, for symmetry reasons, the distances to the plane are identical (± 0.353 Å) and the two carbon atoms are located on opposite sides of the mean plane. In contrast, in the LS state these carbon atoms are located on the same side of the mean plane and at different distances to it (0.872 Å and 0.303 Å).

The inversion of the ethylene conformation and the transformation of the coordination sphere induce significant variations of the intermolecular interactions. In particular, changes of the hydrogen bonds involving the water of solvation, the ethylene carbon atoms and more significantly, of those H-bonds involving the oxygen atoms belonging to the coordination sphere. In the HS state, these two

oxygen atoms do not participate in any intermolecular interaction however, in the LS state the oxygen atom that leaves the coordination sphere forms a hydrogen bond with a methyl group of a neighbouring molecule (O . . . H = 2.33 Å, OCH = 154°). The large changes in the intermolecular contacts are noteworthy since they play an essential role in the propagation of the spin crossover across the solid.

19.4.3.2   Spin Crossover in Fe(II) Phosphine Complexes

One of the most interesting features of the SCO effect is the feasibility of addressing information reversibly in the solid state by light irradiation, according to the well-known Light-Induced Excited-Spin-State Trapping (LIESST) effect and reverse-LIESST effect. However, trapping and keeping the system in the metastable HS state generally requires very low temperatures. The HS $\rightarrow$ LS relaxation process, largely a quantum mechanical tunnelling process, is known to be influenced among other factors, by the differences in metal-ligand bond lengths and differences in energies between the two states. This process has been widely studied, mostly on SCO complexes involving Fe(II) centres with nitrogen donor ligands, as in the previous examples. However, an alternative to nitrogen donor ligands is the use of phosphine ligands.

   [Fe(dppen)$_2$X$_2$]·2S type compounds [dppen = cis-1,2-bis(diphenylphosphino) ethylene; X=Cl, Br; S=CHCl$_3$, CH$_2$Cl$_2$, (CH$_3$)$_2$CO] have been shown to undergo both thermal-, pressure- and light induced spin transitions [97–100]. Single crystal structure determinations have been carried out above and below the SCO transition temperatures for [Fe(dppen)$_2$Cl$_2$]·2(CH$_3$)$_2$CO [97] and [Fe(dppen)$_2$Br$_2$]·2CHCl$_3$ [100]. Both cases have revealed a substantial shortening of the Fe–P bond, an average of 0.28(1) Å, upon conversion from HS to LS, larger than the more common $\sim$0.20 Å contraction in Fe–N bonds [74]. The decrease of the Fe–Halide bond length is an order of magnitude smaller at an average of 0.033(1) Å. The variation of the bond angles in the FeP$_4$Hal$_2$ fragment is also relatively small, as indicated by the $\sim$15% change in the value of the octahedron distortion parameter Σ [96] upon the transition, in comparison to values of 30–55% for FeN$_6$ coordination. Thus, the main structural change upon a spin crossover transition in these complexes is the Fe–P bond lengths. From measurements of the HS $\rightarrow$ LS relaxation curves at different temperatures of the metastable HS state after LIESST, Wu et al. [100] have estimated the temperature independent tunneling rate and correlated them with the transition temperatures $T_{1/2}$ for four FeP$_4$Hal$_2$ complexes. Comparison of this correlation with that of Hauser [101] for FeN$_6$ spin crossover complexes, shows that for a given $T_{1/2}$ value, the FeP$_4$Hal$_2$ complexes exhibit a much slower rate of low-temperature tunneling than the FeN$_6$ complexes. They ascribe this result to the larger bond length changes observed between the HS and LS states.

Fig. 19.12 ORTEP plot of
the cation of TD1 at 170 K.
Ellipsoids at 50% probability.
H atoms have been omitted
for clarity. (Reproduced from
Ref. [7] with kind permission
of The Royal Society of
Chemistry)
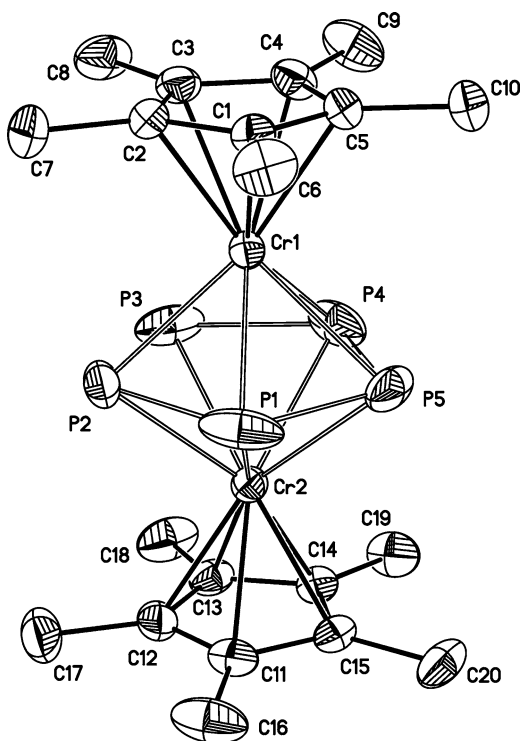
19.4.3.3 Abrupt Rearrangement of the Electron Density in a Dinuclear Cr(II) Spin Crossover System

As mentioned above most structural studies reported on spin crossover concern octahedrally coordinated Fe(II) complexes. However, at least three cases have been reported that include a d^4 metal ion as the magnetic centre [7, 102–104] and only one of them, a triple decker dinuclear Cr(II) complex, shows a metal environment that is not octahedral [7, 102].

$[(Cp^*)Cr(\mu^2{:}\eta^5 - P_5)Cr(Cp^*)]^+$ $(SbF_6)^-$ (TD1), where Cp^* is a pentamethyl-cyclopentadienyl ion, undergoes a sharp SCO at approximately 23 K. The molar susceptibility and the structural results between 290 and 170 K are consistent with 2 non-interacting d^4 Cr^{2+} ions. At these temperatures the asymmeric unit of TD1 (in space group *Fddd*) contains a cation, shown in Fig. 19.12, and an anion. At 290 K the five-membered phosphorus ring (^5P ring) shows an almost continuous ring of electron density. This is attributed to librational disorder, as the electron density separates into discrete atomic entities as the temperature is lowered (Fig. 19.13). The Cr–Cr separation gradually decreases from 3.1928(5) Å at 290 K to 3.1588(4) Å at 170 K. The P–P distances and Cr-P-Cr angles are all similar within this temperature range.
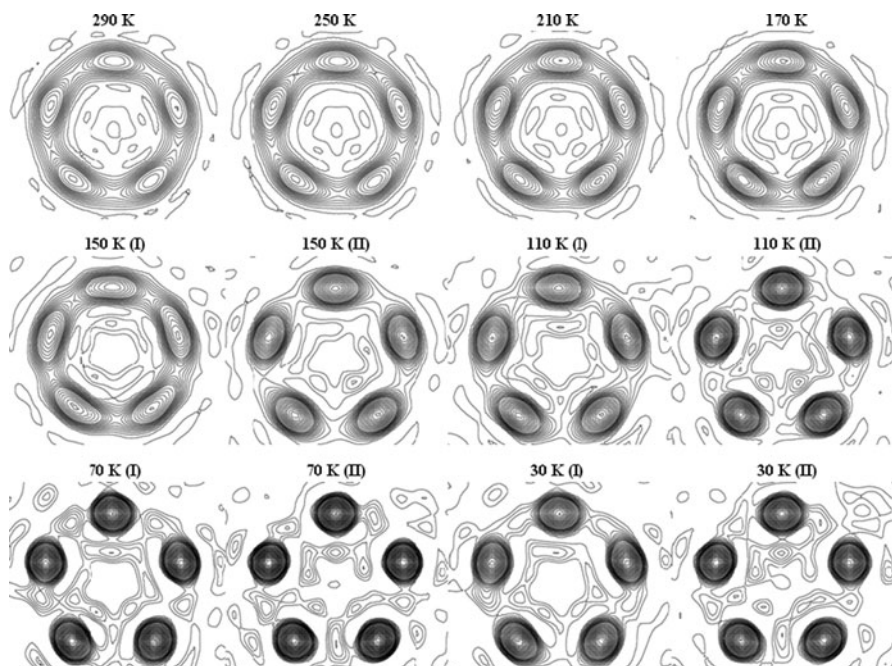
Fig. 19.13 Electron density maps (Fobs) of the five-membered phosphorus ring at different temperatures. Below 160 K there are two crystallographically independent cations in the asymmetric unit, (I) and (II) (Reproduced from Ref. [7] with kind permission of The Royal Society of Chemistry)

A structural phase transition with a change of symmetry is observed at 160 K, from space group *Fddd* to *I2/a*, in parallel with a change shown in the magnetic behaviour between 150 and 25 K. This results in a structure containing 2 independent cations per asymmetric unit. At 150 K the Cr-Cr separations are 3.1201(8) Å for cation I and 3.1657(7) Å for cation II, clearly showing that the geometries of the 2 cations, although similar, are inequivalent. The libration of the ^5P rings is markedly different (Fig. 19.13), cation I still showing a large libration of the ^5P ring but a reduced Cr-Cr distance while cation II, where the libration of the ^5P ring has been dramatically decreased, shows less change in the Cr-Cr separation.

From 150 to 25 K, the Cr-Cr separation decreases for both cations, the change for cation I (~ 0.23 Å) being 4 times that of cation II. The dramatic change between 150 and 25 K in cation I suggests a strong AF interaction, while cation II could still be considered as containing 2 non-interacting Cr^{2+} ions. At 25 K the Cr-Cr separation in cation I is 2.886(2) Å, 0.222 Å smaller than the value of 3.108(2) Å for cation II. All P–P distances and Cr-P-Cr angles are still similar within each cation but clearly different between the 2 symmetry independent cations. The average values at 25 K are 2.225(3) Å and 74.7(2)° for cation I and, 2.200(7) Å and 79.4(3)° for cation II respectively.

The unit cell parameters from 290 K down to 25 K had shown an approximately linear decrease in the volume with temperature. However, they show a sharp change between 20 K and 18 K. Furthermore, a sudden change in the observed intensity of a few monitored reflections can be seen at 24 K, clearly indicating a sudden rearrangement of the electron density. These results are all in accordance with the sharp magnetic transition at 23 K [102], given that small differences in measured transition temperatures can be attributed to differences in temperature calibrations for the different instruments.

No alteration of the symmetry is observed below 25 K however, at 12 K the Cr-Cr separations of the 2 independent cations again become quite similar, at 2.782(2) and 2.798(2) Å. If an AF interaction is assumed between the Cr ions with the shorter Cr–Cr distance at 25 K, it is evident that at 12 K both pairs of Cr ions present an AF interaction. This would make the material diamagnetic, as is observed experimentally [102].

The rearrangement of the electron density below the transition at 23 K is considerable. Below this transition the two ^5P rings become again very similar. However, the P-P distances within each ^5P ring are no longer equivalent. Each ^5P ring distorts and the P-P bonds can be grouped in two short, two medium and a long one. The ^5P rings could then be pictured as consisting of two entities: one group of 3 phosphorus atoms separated by an average distance of 2.165(5) Å and a group of 2 phosphorus atoms separated by an average distance of 2.386(6) Å. The average remaining P-P distance is intermediate at 2.265(10) Å. Concurrently with the ^5P ring distortion the Cr ions move towards the longest P–P bond. Hence, the elongation of a P–P bond in each ring below the magnetic transition could be seen as due to the pronounced η^2-coordination to the Cr ions and/or as a means for the Cr ions to maximise their antiferromagnetic interaction by way of a superexchange interaction through the P atoms. The shift of electron density from a P–P bond to the Cr–P contacts would improve the magnetic coupling between the metal ions. Additionally, at 12 K the Cr ions are found in positions very similar to those formed at 25 K by the cation already showing the suggested AF interaction, with Cr-P-Cr angles in both cations of 74.2(3)°.

This explanation for the shortening of the Cr–Cr distance differs from that suggested by Hughes et al. [102], who explained the magnetic interaction in terms of metal-metal bonding. Their theory would imply that metal d_z^2 orbitals from the Cr atoms are overlapping through the 'hole' in the ^5P ring, forming a M–M sigma bond. The ideal positions for these metal orbitals to overlap are above and below the centroid of the ^5P ring. Hence, this hypothesis does not explain the movement of the Cr atoms away from these ideal positions towards 2 of the phosphorus atoms, after the transition at 23 K.

The observed results may also be interpreted as a two-step spin crossover, a process that has been observed before in dinuclear compounds [105–107]. Given that two non-interacting Cr^{2+} ions with S = 1 will explain the value of 4.1 μ_B for the effective magnetic moment between RT and 160 K, the spin state of a Cr^{2+} ion with S = 1 can be called high spin (HS). Two (or four) non-interacting Cr^{2+} ions with S = 0, i.e. in a low spin state (LS), will explain then a diamagnetic material

below 23 K. But at 25 K, the material can be thought of as having the two Cr^{2+} ions of one cation as non-interacting with $S = 1$ (HS, longer Cr-Cr separation) and the two Cr^{2+} ions of the second independent cation as non-interacting with $S = 0$ (LS, shorter Cr-Cr separation). At all times, within each molecule, the behaviour of each Cr_2P_5 unit is symmetrical, e.g. the distance from each Cr to the centroid of the ^5P rings is the same within experimental error. Hence, instead of having dinuclear units in a HS-LS state, TD1 presents between 160 and 25 K a dinuclear unit in which the Cr^{2+} ions are both in a high spin state, i.e. HS-HS, and a dinuclear unit in which the Cr^{2+} ions are both in a low spin state, i.e. LS-LS. However, explaining the behaviour of TD1 using this theory, would not account for the change in geometry of the ^5P rings below 23 K.

This test case highlights the relevance of performing careful analyses of the electron density distribution. Information obtained simply by following changes in atomic positions through structural transitions cannot provide a complete understanding of magnetic behaviour. A full analysis of the experimental electron density distribution could aid the understanding of the underlying magnetic transition pathways. However, as previously stated, the experiments require the use of very low temperatures and their complexity can be increased by inherent problems such as twinning and the presence of heavy elements, which intrinsically limits this approach. In these cases, combining modern theoretical methods with measured structural data may still provide a route to understanding the correlations between $\rho(\mathbf{r})$ and physical observables.

References

1. Koritsanszky T, Coppens P (2001) Chemical applications of X-ray charge-density analysis. Chem Rev 101:1583–1627
2. Mary TA, Evans JSO, Vogt T, Sleight AW (1996) Negative thermal expansion from 0.3 to 1050 Kelvin in ZrW_2O_8. Science 272:90–92
3. Bader RFW (1990) Atoms in molecules: a quantum theory, vol 22, International series of monographs on chemistry. Oxford Science, Oxford
4. Matta CF, Boyd RJ (eds) (2007) The quantum theory of atoms in molecules: from solid state to DNA and drug design. Wiley-VCH, Weinheim
5. Gütlich P, Garcia Y, Goodwin HA (2000) Spin crossover phenomena in Fe(II) complexes. Chem Soc Rev 29:419–427
6. Hostettler M, Birkedal H, Gardon M, Chapuis G, Schwarzenbach D, Bonin M (1999) Phase-transition-induced twinning in the 1:1 adduct of hexamethylenetetramine and azelaic acid. Acta Crystallogr B 55:448–458
7. Goeta AE, Howard JAK, Hughes AK, O'Hare D, Copley RCB (2007) Structural-magnetic correlations of the first dinuclear spin crossover d^4 system. J Mater Chem 17:485–492
8. Samulon EC, Islam Z, Sebastian SE, Brooks PB, McCourt MK Jr, Ilavsky J, Fisher IR (2006) Low-temperature structural phase transition and incommensurate lattice modulation in the spin-gap compound $BaCuSi_2O_6$. Phys Rev B 73:100407
9. Yang G, Shang P, Jones IP, Abell JS, Gough CE (1993) Monoclinic phase transition and twinning in $Bi_2Sr_2CaCu_2O_y$ single crystals. Phys Rev B 48:16873–16876

10. Lee HJ, Kim KH, Kim MW, Noh TW, Kim BG, Koo TY, Cheong S-W, Wang YJ, Wei X (2002) Optical evidence of multiphase coexistence in single crystalline (La, Pr, Ca)MnO_3. Phys Rev B 65:115118

11. Blaha P, Schwartz K, Madsen GKH, Kvasnicka D, Luitz J (2001) WIEN2K, an augmented plane wave + local orbitals program for calculating crystal properties. Karlheinz Schwarz Techn. Universitat, Wien

12. Kresse G, Marsman M, Furthmüller J (2009) VASP the GUIDE. Universität Wien, Wien

13. Capelli SC, Albinati A, Mason SA, Willis BTM (2006) Molecular motion in crystalline naphtalene: analysis of multi-temperature X-ray and neutron diffraction data. J Phys Chem A 110:11695–11703

14. Bolotina NB, Hardie MJ, Speer RL Jr, Pinkerton AA (2004) Energetic materials: variable-temperature crystal structures of γ- and ε-HNIW polymorphs. J Appl Crystallogr 37:808–814

15. Larsen FK (1995) Diffraction studies of crystals at low temperatures – crystallography below 77 K. Acta Crystallogr B 51:468–482

16. Lo Presti L, Invernizzi D, Soave R, Destro R (2005) Looking for structural phase transitions in the colossal magnetoresistive thiospinel $FeCr_2S_4$ by a multi-temperature single-crystal X-ray diffraction study. Chem Phys Lett 416:28–32

17. Seliger J, Žagar V, Gotoh K, Ishida H, Konnai A, Amino D, Asaji T (2009) Hydrogen bonding in 1,2-diazine-chloranilic acid (2:1) studied by a [14] N nuclear quadrupole coupling tensor and multi-temperature X-ray diffraction. Phys Chem Chem Phys 11:2281–2286

18. Piccoli PMB, Koetzle TF, Schultz AJ, Zhurova EA, Stare J, Pinkerton AA, Eckert J, Hadzi D (2008) Variable temperature neutron diffraction and X-ray charge density studies of tetraacetylethane. J Phys Chem A 112:6667–6677

19. Thomas LH, Cole JM, Wilson CC (2008) Orientational disorder in 4-chloro-nitrobenzene. Acta Crystallogr C 64:o296–o302

20. Parkin A, Adam M, Cooper RI, Middlemiss DS, Wilson CC (2007) Structure and hydrogen bonding in 2,4-dihydroxy-benzoic acid at 90, 100, 110 and 150 K; a theoretical and single-crystal X-ray diffraction study. Acta Crystallogr B 63:303–308

21. Stewart RF (1976) Electron population analysis with rigid pseudoatoms. Acta Crystallogr A 32:565–574

22. Hirshfeld FL (1977) A deformation density refinement program. Isr J Chem 16:226–229

23. Hansen NK, Coppens P (1978) Testing aspherical atom refinements on small-molecule data sets. Acta Crystallogr A 34:909–921

24. Destro R, Pilati T, Simonetta M (1977) The structure and electron density of *sym*-dibenzo-1,5-cyclooctadiene-3,7-diyne by X-ray analysis at three different temperatures. Acta Crystallogr B 33:447–456

25. Coppens P, Becker PJ (1995) International tables for crystallography, vol C. Kluwer Academic Publisher, Dordrecht, p 628

26. Zhurov VV, Zhurova EA, Pinkerton AA (2008) Optimization and evaluation of data quality for charge density studies. J Appl Crystallogr 41:340–349

27. Destro R, Loconte L, Lo Presti L, Roversi P, Soave R (2004) On the role of data quality in experimental charge-density studies. Acta Crystallogr A 60:365–370

28. Pratt Brock C, Dunitz JD, Hirshfeld FL (1991) Transferability of deformation densities among related molecules: atomic multipole parameters from perylene for improved estimation of molecular vibrations in naphthalene and anthracene. Acta Crystallogr B 47:789–797

29. Mata I, Espinosa E, Molins E, Veintemillas S, Maniukiewicz W, Lecomte C, Cousson A, Paulus W (2006) Contributions to the application of the transferability principle and multipolar modelling of H atoms: electron-density study of L-histidinium dihydrogen orthophosphate orthophosphoric acid. I. Acta Crystallogr A 62:365–378

30. Pichon-Pesme V, Lecomte C, Lachekar H (1995) On building a data bank of transferable experimental electron density parameters: application to polypeptides. J Phys Chem 99:6242–6250

31. Jelsch C, Pichon-Pesme V, Lecomte C, Aubry A (1998) Transferability of multipole charge-density parameters: application to very-high resolution oligopeptide and protein structures. Acta Crystallogr D 54:1306–1308

32. Koritsanszky T, Volkov A, Coppens P (2002) Aspherical-atom scattering factors from molecular wave functions. 1. Transferability and conformation dependence of atomic electron densities of peptides within the multipole formalism. Acta Crystallogr A 58:464–472

33. Li N, Maluandes S, Blessing RH, Dupuis M, Moss GR, DeTitta GT (1994) High-resolution X-ray diffraction and *ab initio* quantum chemical studies of glycouril, a biotin analog. J Am Chem Soc 116:6494–6507

34. Oddershede J, Larsen S (2004) Charge density study of naphtalene based on X-ray diffraction data at four different temperatures and theoretical calculations. J Phys Chem A 108:1057–1063

35. Macchi P, Proserpio DM, Sironi A, Soave R, Destro R (1998) A test of the suitability of CCD area detectors for accurate electron-density studies. J Appl Crystallogr 31:583–588

36. Messerschmidt M, Scheins S, Luger P (2005) Charge density of (−)-stricnine from 100 to 15 K, a comparison of four data sets. Acta Crystallogr B 61:115–121

37. Overgaard J, Clausen HF, Platts JA, Iversen BB (2008) Experimental and theoretical charge density study of chemical bonding in a Co dimer complex. J Am Chem Soc 130:3834–3843

38. Overgaard J, Larsen FK, Timco GA, Iversen BB (2009) Experimental charge density in an oxidized trinuclear iron complex using 15 K synchrotron and 100 K conventional single-crystal X-ray diffraction. Dalton Trans 664–671

39. Lippmann T, Schneider JR (2000) Topological analyses of cuprite, Cu_2O, using high-energy synchrotron-radiation data. Acta Crystallogr A 56:575–584

40. Kirfel A, Lippmann T, Blaha P, Schwarz K, Cox DF, Rosso KM, Gibbs GV (2005) Electron density distribution and bond critical point properties for forsterite, Mg_2SiO_4, determined with synchrotron single crystal X-ray diffraction data. Phys Chem Miner 32:301–313

41. Kirfel A, Krane H-G, Blaha P, Schwarz K, Lippmann T (2001) Electron density distribution in stishovite, SiO_2: a new high-energy synchrotron-radiation study. Acta Crystallogr A 57:663–677

42. O'Toole NJ, Streltsov VA (2001) Synchrotron X-ray analysis of the electron density in CoF_2 and ZnF_2. Acta Crystallogr B 57:128–135

43. Hansen NK, Schneider JR, Yelon WB, Pearson WH (1987) The electron density of beryllium derived from 0.12 Å γ-ray diffraction data. Acta Crystallogr A 43:763–769

44. Scheringer C (1980) The electron-density distribution in silicon. Acta Crystallogr A 36:205–210

45. Spackman MA, Hill RJ, Gibbs GV (1987) Exploration of structure and bonding in stishovite with fourier and pseudoatom refinement methods using single crystal and powder X-ray diffraction data. Phys Chem Miner 14:139–150

46. Gibbs GV, Cox DF, Rosso KM, Kirfel A, Lippmann T, Blaha P, Schwarz K (2005) Experimental and theoretical bond critical point properties from model electron density distributions for earth materials. Phys Chem Mater 32:114–125

47. Destro R, Marsh RE, Bianchi R (1988) A low-temperature (23 K) study of L-alanine. J Phys Chem 92:966–973

48. Destro R, Bianchi R, Gatti C, Merati F (1991) Total electronic charge density of L-alanine from X-ray diffraction at 23 K. Chem Phys Lett 186:47–52

49. Destro R, Soave R, Barzaghi M (2008) Physicochemical properties of zwitterionic L- and DL-alanine crystals from their experimental and theoretical charge densities. J Phys Chem B 112:5163–5174

50. Hübschle CB, Luger P (2006) MolIso – a program for colour-mapped iso-surfaces. J Appl Crystallogr 39:901–904

51. Barzaghi M (2002) PAMoC Online user's manual. CNR-ISTM, Institute of Molecular Science and Technologies, Milano. http://www.istm.cnr.it/pamoc/

52. Volkov A, Coppens P (2004) Calculation of electrostatic interaction energies in molecular dimers from atomic multipole moments obtained by different methods of electron density partitioning. J Comput Chem 25:921–934

53. Volkov A, Koritsanszky T, Coppens P (2004) Combination of the exact potential and multipole methods (EP/MM) for evaluation of intermolecular electrostatic interaction energies with pseudoatom representation of molecular electron densities. Chem Phys Lett 391:170–175

54. Dovesi R, Saunders VR, Roetti C, Orlando R, Zicovich-Wilson CM, Pascale F, Civalleri B, Doll K, Harrison NM, Bush IJ, D'Arco Ph, Llunell M (2006) CRYSTAL06 user's manual. Università di Torino, Torino

55. Poulsen RD, Bentien A, Christensen M, Iversen BB (2006) Solvothermal syntesis, multi-temperature crystal structures and physical properties of isostructural coordination polymers, $2C_4H_{12}N^+$-$[M_3(C_8H_4O_4)_4]^{2-}$·$3C_5H_{11}NO$, M = Co, Zn. Acta Crystallogr B 62:245–254

56. Poulsen RD, Bentien A, Chevalier M, Iversen BB (2005) Synthesis, physical properties, multitemperature crystal structure, and 20 K synchrotron X-ray charge density of a magnetic metal organic framework structure, $Mn_3(C_8O_4H_4)_3(C_5H_{11}ON)_2$. J Am Chem Soc 127:9156–9166

57. Tanaka K, Ōnuki Y (2002) Observation of $4f$ electron transfer from Ce to B_6 in the Kondo crystal CeB_6 and its mechanism by multi-temperature X-ray diffraction. Acta Crystallogr B 58:423–436

58. Zhurova EA, Tsirelson VG, Zhurov VV, Stash AI, Pinkerton AA (2006) Chemical bonding in pentaerythritol at very low temperature or at high pressure: an experimental and theoretical study. Acta Crystallogr B 62:513–520

59. Tanaka K (1988) X-ray analysis of wavefunctions by the least-squares method incorporating orthonormality. I. General formalism. Acta Crystallogr A 44:1002–1008

60. Tanaka K (1993) X-ray analysis of wavefunctions by the least-squares method incorporating orthonormality. II. Ground state of the Cu^{2+} ion of bis(1,5-diazacyclooctane)copper(II) nitrate in a low-symmetry crystal field. Acta Crystallogr B 49:1001–1010

61. Stezowski JJ (1980) Phase transition effects: a crystallographic characterization of the temperature dependency of the crystal structure of the 1:1 charge transfer complex between anthracene and tetracyanobenzene in the temperature range 297 to 119 K. J Chem Phys 73:538–547

62. Boeyens JCA, Levendis DC (1984) Static disorder in crystals of anthracene-tetracyanobenzene charge transfer complex. J Chem Phys 80:2681–2688

63. Luty T, Munn RW (1984) Theory of phase transitions in charge-transfer complexes: anthracene-tetracyanobenzene. J Chem Phys 80:3321–3327

64. Lefebvre J, Odou G, Muller M, Mierzejewski A, Luty T (1989) Characterization of an orientational disorder in two charge-transfer complexes: anthracene-tetracyanobenzene (A–TCNB) and naphthalene-tetracyanobenzene (N–TCNB). Acta Crystallogr B 45:323–336

65. Lefebvre J, Ecolivet C, Bourges P, Mierzejewski A, Luty T (1991) The structural phase transition in anthracene-TCNB. Phase Transit 32:223–234

66. Dressel M (2007) Ordering phenomena in quasi-one-dimensional organic conductors. Naturwissenschaften 94:527–541

67. Oison V, Katan C, Rabiller P, Souhassou M, Koenig C (2003) Neutral-ionic phase transition: a thorough *ab initio* study of TTF–CA. Phys Rev B 67:035120

68. García P, Dahaoui S, Katan C, Souhassou M, Lecomte C (2007) On the accurate estimation of intermolecular interactions and charge transfer: the case of TTF-CA. Faraday Discuss 135:217–235

69. Oison V, Rabiller P, Katan C (2004) Theoretical investigation of the ground-state properties of DMTF–CA: a step toward the understanding of charge transfer complexes undergoing the neutral-to-ionic phase transition. J Phys Chem A 108:11049–11055

70. Ivanov Y, Nimura T, Tanaka K (2004) Electron density and electrostatic potential of $KMnF_3$: a phase-transition study. Acta Crystallogr B 60:359–368

71. Lo Presti L, Soave R, Destro R (2003) The fungal metabolite austdiol. Acta Crystallogr C 59:o199–o201

72. Lo Presti L, Soave R, Destro R (2006) On the interplay between CH···O and OH···O interactions in determining crystal packing and molecular conformation: an experimental and theoretical charge density study of the fungal secondary metabolite austdiol ($C_{12}H_{12}O_5$). J Phys Chem B 110:6405–6414

73. Whitten AE, Turner P, Klooster WT, Piltz RO, Spackman MA (2006) Reassessment of large dipole moment enhancements in crystals: a detailed experimental and theoretical charge density analysis of 2-methyl-4-nitroaniline. J Phys Chem A 110:8763–8776

74. Gütlich P, Goodwin HA (eds) (2004) Spin crossover in transition metal compounds. Topics in current chemistry, vols 233–235. Springer, New York and references therein

75. Lecomte C, Chadwick DL, Coppens P, Stevens ED (1983) Electronic structure of metalloporphyrins. 2. Experimental electron density distribution of (meso-tetraphenylporphinato) iron(III) methoxide. Inorg Chem 22:2982–2992

76. Coppens P, Li L (1984) Electron density studies of porphyrins and phthalocyanines. III. The electronic ground state of iron(II) phthalocyanine. J Chem Phys 81:1983–1993

77. Tanaka K, Elkaim E, Liang L, Zhu NJ, Coppens P, Landrum J (1986) Electron density studies of porphyrins and phthalocyanines. IV. Electron density distribution in crystals of (meso-tetraphenylporphinato) iron(II). J Chem Phys 84:6969–6978

78. Lecomte C, Blessing RH, Coppens P, Tabard A (1986) Electron density studies of porphyrins and phthalocyanines. 5. Electronic ground state of iron(II) tetraphenylporphyrin bis(tetrahydrofuran). J Am Chem Soc 108:6942–6950

79. Elkaim E, Tanaka K, Coppens P, Scheidt RW (1987) Low temperature study of bis(2-methylimidazole)(octaethylporphinato) iron(III) perchlorate. Acta Crystallogr B 43:457–461

80. Li N, Coppens P, Landrum J (1988) Electron density studies of porphyrins and phthalocyanines. 7. Electronic ground state of bis(pyridine)(meso-tetraphenylporphinato) iron(II). Inorg Chem 27:482–488

81. Milne AM, Maslen EN (1988) Electron density in the spin crossover complex trans-[N, N'-ethylenebis(salicylideneaminato)]bis(imidazole)iron(III) perchlorate. Acta Crystallogr B 44:254–259

82. Pillet S, Legrand V, Weber HP, Souhassou M, Létard JF, Guionneau P, Lecomte C (2008) Out-of-equilibrium charge density distribution of spin crossover complexes from steady-state photocrystallographic measurements: experimental methodology and results. Z Kristallogr 223:235–249

83. Legrand V, Pillet S, Souhassou M, Lugan N, Lecomte C (2006) Extension of the experimental electron density analysis to metastable states: a case example of the spin crossover complex $Fe(btr)_2(NCS)_2 \cdot H_2O$. J Am Chem Soc 128:13921–13931

84. Vreugdenhil W, Van Diemen JH, De Graaf RAG, Haasnoot JG, Reedijk J, Van Der Kraan AM, Kahn O, Zarembowitch J (1990) High-spin $\leftrightarrow$ low-spin transition in [Fe(NCS)$_2$(4,4'-bis-1,2,4-triazole)$_2$](H$_2$O). X-ray crystal structure and magnetic, mössbauer and epr properties. Polyhedron 9:2971–2979

85. Pillet S, Hubsch J, Lecomte C (2004) Single crystal diffraction analysis of the thermal spin conversion in [Fe(btr)$_2$(NCS)$_2$]·H$_2$O: evidence for spin-like domain formation. Eur J Phys B 38:541–552

86. Legrand V (2005) Cristallographie et photo-cristallographie haute résolution de matériaux à transition de spin: propriétés structurales, électroniques et mécanismes de conversion. PhD thesis, University Henri Poincaré, Nancy I

87. Holladay A, Leung P, Coppens P (1983) Generalized relations between d-orbital occupancies of transition metal atoms and electron density multipole population parameters from X-ray diffraction data. Acta Crystallogr A 39:377–387

88. Stevens ED, Coppens P (1979) Refinement of metal d-orbital occupancies from X-ray diffraction data. Acta Crystallogr A 35:536–539

89. Coppens P (1997) X-Ray charge densities and chemical bonding, International union of crystallography texts on crystallography series. Oxford University Press, Oxford

90. Rees B, Mitschler A (1976) Electronic structure of chromium hexacarbonyl at liquid nitrogen temperature. 2. Experimental study (X-ray and neutron diffraction) of σ and π bonding. J Am Chem Soc 98:7918–7924

91. Abramov YA (1997) On the possibility of kinetic energy density evaluation from the experimental electron density distribution. Acta Crystallogr A 53:264–272

92. Bader RFW, Essen H (1984) The characterization of atomic interactions. J Chem Phys 80:1943–1960

93. Bianchi R, Gatti C, Adovasio V, Nardelli M (1996) Theoretical and experimental (113 K) electron density study of lithium bis(tetramethylammonium) hexanitrocobaltate(III). Acta Crystallogr B 52:471–478

94. Macchi P, Sironi A (2003) Chemical bonding in transition metal carbonyl clusters: complementary analysis of theoretical and experimental electron densities. Coord Chem Rev 238–239:383–412

95. Guionneau P, Le Gac F, Kaiba A, Sánchez Costa J, Chasseau D, Létard JF (2007) A reversible metal-ligand bond break associated to a spin-crossover. Chem Commun 3723–3725

96. Guionneau P, Marchivie M, Bravic G, Létard JF, Chasseau D (2004) Structural aspects of spin crossover. Example of the $[Fe^{II}L_n(NCS)_2]$ complexes. In: Gütlich P, Goodwin HA (eds) Topics in current chemistry, vol 234. Springer, Berlin, pp 97–128

97. Cecconi F, Di Vaira M, Midollini S, Orlandini A, Sacconi L (1981) Singlet ↔ quintet spin transitions of iron(II) complexes with a P_4Cl_2 donor set. X-Ray structures of the compound $FeCl_2(Ph_2PCH = CHPPh_2)_2$ and of its acetone solvate at 130 K and 295 K. Inorg Chem 20:3423–3430

98. Di Vaira M, Midollini S, Sacconi L (1981) Low spin and high spin six-coordinate iron(II) complexes with a P_4Cl_2 donor set. X-Ray structures of $FeCl_2[(Ph_2PCH_2CH_2)_2PPh]_2 \cdot 2(CH_3)_2CO$ and of $FeCl_2(Me_2PCH_2CH_2PMe_2)_2$. Inorg Chem 20:3430–3435

99. McCusker JK, Zvagulis M, Drickamer HG, Hendrickson DN (1989) Pressure-induced spin-state phase transitions in $Fe(dppen)_2Cl_2$ and $Fe(dppen)_2Br_2$. Inorg Chem 28:1380–1384

100. Wu C-C, Jung J, Gantzel PK, Gütlich P, Hendrickson DN (1997) LIESST effect studies of iron(II) spin-crossover complexes with phosphine ligands: relaxation kinetics and effects of solvent molecules. Inorg Chem 36:5339–5347

101. Hauser A (1991) Intersystem crossing in Fe(II) coordination compounds. Coord Chem Rev 111:275–290

102. Hughes AK, Murphy VJ, O'Hare D (1994) Synthesis, X-ray structure and spin crossover in the triple-decker complex $[(\eta^5-C_5Me_5)Cr(\mu^2:\eta^5-P_5)Cr(\eta^5-C_5Me_5)]^+[A]^-$ (A = PF_6, SbF_6). J Chem Soc Chem Commun 163–164

103. Sim PG, Sinn E (1981) First manganese(III) spin crossover and first d^4 crossover. Comment on cytochrome oxidase. J Am Chem Soc 103:241–243

104. Halepoto DM, Holt DGL, Larkworthy LF, Jeffery Leigh G, Povey DC, Smith GW (1989) Spin crossover in chromiun(II) complexes and the crystal and molecular structure of the high spin form of bis[1,2-bis(diethylphosphino)ethane] di-iodochromiun(II). J Chem Soc Chem Commun 1322–1323

105. Real JA, Gaspar AB, Muñoz MC, Gütlich P, Ksenofontov V, Spiering H (2004) Bipyrimidine-bridged dinuclear iron(II) spin crossover compounds. In: Gütlich P, Goodwin HA (eds) Topics in Current Chemistry, vol 233. Springer, Berlin, pp 167–193 and references therein

106. Amoore JLM, Kepert CJ, Cashion JD, Moubaraki B, Neville SM, Murray KS (2006) Structural and magnetic resolution of a two-step full spin-crossover transition in a dinuclear iron(II) pyridil-bridged compound. Chem Eur J 12:8220–8227

107. Kaiba A, Shepherd HJ, Fedaoui D, Rosa P, Goeta AE, Rebbani N, Létard JF, Guionneau P (2010) Crystallographic elucidation of purely structural, thermal and light-induced spin transitions in an iron(II) binuclear complex. Dalton Trans 39:2910–2918